MO-PECVD (METAL-ORGANIC PLASMA ENHANCED CHEMICAL VAPOUR DEPOSITION) OF ERBIUM-DOPED HYDROGENATED AND DEUTERATED AMORPHOUS CARBON

By

Raymond Tsai

A thesis submitted in conformity with the requirements for the Degree of Master of Applied Science
Graduate Department of The Edward S. Rogers Sr. Department of Electrical and Computer Engineering, University of Toronto

© Copyright by Raymond Tsai (2008)

MO-PECVD (Metal-Organic Plasma Enhanced Chemical Vapour Deposition) of Erbium-Doped Hydrogenated and Deuterated Amorphous Carbon

Master of Applied Science (2008)
Raymond Tsai

Graduate Department of the Edward S. Rogers Sr. Department of Electrical and Computer Engineering, University of Toronto

Abstract

Erbium (Er^{3+}) ion has been widely used in silica fiber-based active photonic devices, given its characteristic emission around 1.5 μm. Hydrogenated and deuterated amorphous carbon (a-C:H and a-C:D, respectively), thin film materials offering tailorable opto-electronic properties, have not been explored thoroughly as host materials for Er. The objective of this research is to study the potential suitability of a-C:H and a-C:D as Er^{3+} hosts for 1.54 μm light emitting applications. Erbium-doped hydrogenated amorphous carbon (a-C:H(Er)) is fabricated through controlled thermal evaporation of metal-organic compounds in a hydrocarbon discharge generated by the DC saddle-field plasma enhanced chemical vapour deposition system. Er photoluminescence (PL) is successfully demonstrated for the first time in Er-doped deuterated amorphous carbon (a-C:D(Er)). Uniform distribution of optically active Er^{3+} ions is attained by using tris(2,2,6,6-tetramethy1-3-5-heptanedionate)Erbium(III) ($Er(thd)_3$) compound as revealed by XPS analysis. $Er(thd)_3$ is observed to be a preferred dopant over Erbium(III) 2,4-pentanedionate ($Er(acac)_3$). Deuteration of amorphous carbon has effectively removed the PL quenching effect caused by non-radiative C-H and O-H vibrational transitions. An improvement factor of ~ 4.4 is observed in the minimum doping level of Er required to attain PL in a-C:D(Er), compared to a-C:H(Er). The results of this thesis suggest that a-C:D(Er) material can potentially be used for silicon-compatible opto-electronics applications in 1.5 μm region.

// Acknowledgements

First and foremost, I would like to acknowledge and thank my supervisors, Professors N. P. Kherani and L. Qian for their guidance, support, and understanding during this research work. It has been a privilege to work with them. I am indebted to Professor Qian for her endless support in the construction of photoluminescence spectroscopy system and to Professor Kherani for providing a supportive environment in which this research was conducted. I am grateful to Professor E. H. Sargent and Dr. Vlad Sukhovatkin for giving me access to their spectrometer and the assistance they lent us during the photoluminescence measurements. I would also like to thank the committee members, Professors E. H. Sargent, P. R. Herman, A. S. Helmy and K. G. Balmain for their time, expertise and helpful critiques.

I would like to express my great gratitude to Drs. Davit Yeghikyan and Tome Kosteski for their assistance with the DC Saddle-Field PECVD system. I am grateful to Keith Leong for instructing me on operating of deposition system and for providing an unlimited amount of help of many characterization measurements. Special thanks to Dr. P. Brodersen for performing XPS analysis. I am also thankful to my colleagues Pratish Mahtani, Paul O'Brien and Barzin Bahardoust for their assistance and friendship.

Finally, I would like to thank Mom, Steve and NiNi. Without your support, I would have never made this far.

Table of Contents Page

Abstract ii
Acknowledgements iii
Table of contents iv
List of Figures vi
List of Tables ix
List of Symbols, and Acronyms, and Abbreviations x

Chapter 1. Introduction 1

Chapter 2. Hydrogenated Amorphous Carbon (a-C:H)
2.1 Introduction 6
2.2 Various forms of carbon 6
2.3 Role of hydrogen 7
2.4 Hydrogenated amorphous carbon 8

Chapter 3. Metal-organic Erbium Complex
3.1 Introduction 10
3.2 Erbium free-ion and crystal-field perturbations 11
3.3 Erbium-containing β-diketonate complex 13

Chapter 4. Sample Preparation
4.1 Introduction 19
4.2 Conventional thin film deposition techniques 19
4.2.1 Chemical vapour deposition 19
4.2.2 DC glow discharge 21
4.2.3 RF glow discharge 25
4.3 DC saddle-field glow discharge system 26
4.4 Thermal evaporator assembly 29
4.5 Substrate and chamber preparation 31
4.6 Deposition procedure and deposition parameters 33
4.7 Preparation of tris(2,2,6,6-tetramethy1-3-5-heptanedionate) Erbium(III) ($Er(thd)_3$) in KBr and organic solvents 39

Chapter 5. Experimental Characterization Techniques
5.1 Introduction 40

5.2 Film thickness measurement 41
5.3 Ultraviolet and visible absorption 42
5.4 X-ray photoelectron and spectroscopy 44
5.5 Time-of-flight secondary ion mass spectrometry 47
5.6 Photoluminescence spectroscopy 51

Chapter 6. Erbium Complex Doped Amorphous Carbon: Results and Discussion

6.1 Hydrogenated amorphous carbon doped with Erbium(III) 2,4-pentanedionate ($Er(acac)_3$) 53
6.2 Luminescence of $Er(thd)_3$ in KBr pellet and in methanol 57
6.3 Hydrogenated amorphous carbon doped with $Er(thd)_3$ 58
6.4 Luminescence quenching effect 73
6.5 Effect of deuterated material system on Er^{3+} emission 75
6.6 Oxidation state of Er ions 79

Chapter 7. Conclusion and Future Work

7.1 Conclusion 81
7.2 Future work 84

References

List of Figures

Figure 3.1: Schematic representation of the Stark-split Er^{3+} electronic energy levels, showing excitation at 0.98 and 1.48, followed by rapid non-radiative relaxation and emission at 1.54 μm.

Figure 3.2: Three different mechanisms for energy transfer in lanthanide complexes.

Figure 3.3: Molecular structure of tris(2,2,6,6-tetramethy1-3-5-heptanedionate) Erbium(III).

Figure 4.1: A common implementation of CVD (AX, H2, HX – gases, A – solid material).

Figure 4.2: Current-voltage characteristics in a DC glow discharge.

Figure 4.3: Luminous zones and dark spaces in a DC glow discharge.

Figure 4.4: The potential distribution in a DC glow discharge (V_P - plasma potential, V_C – cathode potential).

Figure 4.5: A schematic diagram of the modified DC saddle-field glow discharge deposition.

Figure 4.6: The plasma assisted chemical vapour deposition device for the deposition of carbon layers from methane and erbium metal-organic.

Figure 4.7: The time sequence of experimental actions. The terms t_0 to t_5 are explained in the text: T_S is the substrate temperature, f_{CH_4} the methane flow, T_{Er} the evaporator temperature, and P_{DC} the DC power supplied by the DC power supply.

Figure 5.1: The thickness of a thin film can be measured using a profilometer.

Figure 5.2: The procedure to create a film step.

Figure 5.3: Tauc plot for an undpoed a-C:H sample in the present study. The dashed line shows that the extrapolated Tauc gap is 2.8 eV.

Figure 5.4: XPS emission for a model atom.

Figure 5.5: ToF-SIMS, Primary ion strikes the sample surface and yields secondary particles (atoms, ions, and molecules).

Figure 5.6: Photoluminescence Spectroscopy apparatus.

Figure 6.1: Ramping of evaporator temperature and cumulative $Er(acac)_3$ powder consumption as a function of deposition time for sample B1.

Figure 6.2: SIMS result for sample B1.

Figure 6.3: SIMS result indicates the contaminations.

Figure 6.4: Comparison of emission spectra of $Er(thd)_3$ in KBr and methanol.

Figure 6.5: Evaporator temperature ramping for sample E1.

Figure 6.6: Depth profile of sample E1 as determined by SIMS.

Figure 6.7: C, Si, O, Er and O concentrations as a function of the depth from the film surface as determined by XPS (sample E2).

Figure 6.8: PL spectra for the annealed and non-annealed samples of deposition of E3.

Figure 6.9: Tauc plot of sample E3 annealed at different temperature in H_2; the optical bandgaps determined by extrapolation of the linear portion of the curves to the intercepts on the abscissa.

Figure 6.10: A picture of sample E4.

Figure 6.11: Growth rate of the films as a function of Er concentration.

Figure 6.12: O/Er ratio in the films as a function of Er concentration.

Figure 6.13: C, Si, O, Er and O concentrations as function of the distance from the film surface as determined by XPS (sample E4).

Figure 6.14: C, Si, O, Er and O concentrations as function of the distance from the film surface as determined by XPS (sample E5a).

Figure 6.15: C, Si, O, Er and O concentrations as function of the distance from the film surface as determined by XPS (sample E5b).

Figure 6.16: C, Si, O, Er and O concentrations as function of the distance from the film surface as determined by XPS (sample E6).

Figure 6.17: A picture of sample E7; the arrow marks the spot to the right of which the film exhibits Er luminescence.

Figure 6.18: PL spectrum for the films with Er concentration of 2.0 atm.%.

Figure 6.19: Schematic presentation of the vibrational energy levels in organic media and matching the electronics energy gap of Er^{3+} ion.

Figure 6.20: Comparison with PL spectra for 1.1 mol% of $Er(thd)_3$ in methanol and that in deuterated methanol.

Figure 6.21: A picture of Er-doped a-C:D with an increasing film thickness and Er concentration from right to left.

Figure 6.22: PL spectra of the four spots (see Fig. 6.21) with different Er concentrations in Er-doped a-C:D film.

Figure 6.23: Tauc plot of the Er-doped a-C:D film from which the optical bandgap is extracted.

Figure 6.24*:* Er 4d XPS spectra of four spots on a-C:D(Er) film, $Er(thd)_3$ film (prepared by evaporating the powder) and $Er(thd)_3$ powder. Each spectrum is normalized to its maximum intensity after a background subtraction and offset vertically for clarity of presentation.

List of Tables

Table 2.1: Properties of various forms of carbon.

Table 4.1: Deposition parameters for the diamond-like carbon film.

Table 4.2: Deposition parameters for the set of ten Er doped a-C:H films deposited using the gas mixture (methane + $Er(acac)_3$).

Table 4.3: Deposition parameters for the set of seven Er doped a-C:H films deposited using the gas mixture (methane + $Er(thd)_3$).

Table 5.1: Summary of XPS capabilities and limitations.

Table 6.1: Amount of $Er(acac)_3$ evaporated during each of the depositions.

Table 6.2: Summary of characterization results of sample E2 – E6.

Table 6.3: Summary of atomic concentration results of Er-doped a-C:D sample.

List of Symbols, Acronyms and abbreviations

α – absorption coefficient
a-C:H – hydrogenated amorphous carbon
a-C:D – deuterated amorphous carbon
a-C:H(Er) – erbium-doped a-C:H
a-C:D(Er) – erbium-doped a-C:D
acac – acetylacetonate
AEX – Auger electron spectroscopy
ASF – atomic sensitivity factor
BE – binding energy
C_A – atomic concentration of a given element
CD_3OD – deuterated methanol
CD_4 – deuterated methane
CH_3OH – methanol
CH_4 – methane
CMOS – complementary metal-oxide-semiconductor
CVD – chemical vapour deposition
Cz – Czochralski
d – thickness of film
DCSF – DC saddle-field
E – photon energy
E_B – energy of involved bound electron state
ECR – electron-cyclotron resonance
EDFA – Erbium-doped fiber amplifiers
EDX – energy dispersive analysis
E_g – optical bandgap
E_{KE} – energy of ejected electron
EL – electroluminescence
E_m – lanthanide energy level higher than ligand T_1
E_n – lanthanide energy level lower than ligand T_1
$Er(acac)_3$ – Erbium(III) 2,4-pentanedionate
$Er(hfa)_3$*DME – hfa = $CF_3C(O)CHC(O)CF_3$, DME = $CH_3OCH_2CH_2OCH_3$)
$Er(thd)_3$ – Tris(2,2,6,6-tetramethy1-3-5-heptanedionate)Erbium(III)
$h\nu$ – energy of incident photon
LED – light-emitting diode
MBE – molecular beam epitaxy
M_D – minimum doping requirement for detectable Er emission in a-C:D(Er)

M_H – minimum doping requirement for detectable Er emission in a-C:H(Er)
MOCVD – metal-organic chemical vapour deposition
Nc-Si – silicon nanocrystal
N_i – counts of XPS peak area of a given element
PECVD – plasma enhanced chemical vapour deposition
PID – proportional, integral and derivative
PL – photoluminescence
QE – quantum efficiency
R – reflectance
REE – rare earth element
S_1 – lowest singlet excited states of ligand
S_i – ASF of a given element
SIMS – secondary ion mass spectrometry
SRSO – silicon-rich silicon oxide
T – transmittance
thd – dipivaloylmethane or (2,2,6,6-tetramethy1-3-5-heptanedionate)
T_1 – lowest triplet excited states of ligand
T_A – annealing temperature
ToF-SIMS– time-of-fight secondary ion mass spectrometry
V_c – cathode potential
V_p – plasma potential
XPS – X-ray photoelectron spectroscopy
W – work function

Chapter 1

Introduction

Currently, there is a gap between the silicon-based electronics/computing industry and the III-V semiconductor-based opto-electronics/optical communications industry: Silicon cannot be readily made to emit or amplify light (due to the indirect nature of its bandgap); and, high-speed photonic devices made out of III-V semiconductors are incompatible with silicon. III-V semiconductor-based lasers are fabricated using very different technologies (e.g. MBE and MOCVD) from those for silicon devices (e.g. standard epitaxy). Bringing light onto the silicon chip requires bulky lossy waveguide-to-fiber and fiber-to-waveguide coupling, and the packaging for lasers involves separate lengthy processes. These problems limit practical integration of active photonic and electronic devices, which otherwise would allow high-speed photonic devices to dramatically increase signal processing speed by employing multiple wavelength channels [1].

This project aims to bridge this gap by investigating silicon-compatible materials for light emitting and light-amplifying materials, which could be made into silicon-compatible light emitting diodes, lasers, optical amplifiers, switches, and other active photonic devices. Silicon-compatible materials may provide a platform for future hybrid photonic-electronic integrated circuits, which will not only result in much more compact devices, eliminating many practical problems related to opto-electronic packaging and waveguide coupling, but will also open up possibilities for new combinations and functions previously impossible to achieve.

Currently, there are no silicon-based materials that can be used to make practical lasers and amplifiers operating at 1.54 μm, however, many groups have done extensive research in this vein and have identified few a potential materials. The most promising being the Er embedded in solid matrices has attracted increasing attention since the first report on Er luminescence in silicon in 1983 [2]. Other than silicon, Tsybeskov et al. demonstrated room-temperature photoluminescence (PL) at ~ 1.54 μm in Er-doped silicon-rich silica in 1997 [3]. The decrease in PL from 12 K to 300 K was less than 50 %. The PL spectrum reveals no luminescence bands related to silicon-bandedge recombination, point defects, or dislocations and shows that the Er^{3+} centers are the most efficient radiative recombination centers. They also fabricated a light-emitting diode (LED) with an active layer made of this material, and subsequently electroluminescence (EL) at ~ 1.54 μm was demonstrated [3]. However, the estimated quantum efficiency at that point was still too low for practical device application.

The discovery of selective visible light emission and absorption from nanocrystalline group IV materials has attracted considerable experimental effort to understand its origin and to utilize it to fabricate Si-based optoelectronic devices [4-7]. This novel idea has stimulated another great deal of research interest in nanocrystal Si (nc-Si) sensitization of Er doped silica, in which the Si-nc is pumped by a visible light source, leading to the excitation of Er ion due to energy transfer from nc-Si, and subsequent luminescence. Polman et al. were among the first few groups that observed and studied the indirect excitation of Er by silicon-nanocrystals in silica produced by ion implantation [8]. They observed an increase in effective erbium excitation cross-section by several orders of magnitude due to silicon-nanocrystal sensitization, and demonstrated efficient (~55%) energy transfer from

silicon-nanocrystals to erbium. Iacona et al. observed room-temperature electroluminescence at 1.54 μm from an erbium-doped silicon nanocluster-based MOS device [9]. Lee et al. recently demonstrated on-off optical gain from a waveguide device based on silicon-nanocrystal sensitized erbium-doped silica using a top-pumping 470 nm LED [10]. In both [9] and [10], the samples were produced by conventional PECVD (plasma enhanced chemical vapour deposition) processes.

Other than crystalline Si and silica, it was shown that photo- or electroluminescence at 1.54 μm exists in hydrogenated amorphous silicon, in most A3B5 compounds, silicon carbide [11], in Er-doped Si1-yCy alloys grown by molecular beam epitaxy with y values up to 0.1 [12], and Er-doped hydrogenated amorphous carbon (a-C:H) produced by magnetron sputtering [13]. Among these materials, Er-doped a-C:H has not been explored thoroughly and the mechanism of PL of Er in a-C:H is not clear and not well-understood. Nevertheless, the potential suitability of a-C:H as a host material for Er is worthwhile to study due to its flexibility in the opto-electronic properties: (1) compatible with silicon and silica; (2) low optical absorption in the infrared spectral region; (3) conductive by doping with group III and V elements and tailorable optical gap in the 0.9 – 3.5 eV range; (4) high optical surface quality film with a tailorable refractive index in the 1.47 – 2.76 range.

In [13], the only paper that reported on PL in a-C:H(Er), the deposition process was studied in order to optimize the deposition parameters to obtain higher light emission from Er. The results showed that the luminescence intensity was very low in spite of the concentration of Er being in an acceptable range and the high excitation power. They reported that the low efficiency of the a-C:H(Er) films is related to both the low optical gap, and non-radiative relaxation induced by C-H vibrations. They

were unable to deposit a high optical gap a-C:H(Er) film with acceptable Er concentration. Two possible reasons may address this undesired problem. Firstly, defects that are caused by Er ions embedded in a-C:H network can introduce additional mid-gap energy sates in the material system, and hence reduce the optical gap. Secondly, a-C:H film in [13] was produced by magnetron sputtering of a graphite target, partially covered by metallic erbium, in an atmosphere of argon and C_6H_{12}. In this deposition technique, the Er concentration in the film depends on the degree of sputtering of Er target; high flux and high energy of ions reaching Er target results in high Er concentration, whereas, the optical gap of the a-C:H film decreases with increasing ion energy. If the second mechanism is the dominating factor producing low optical gap, it is desirable to seek an alternative method with independent control over the incorporation of Er into a-C:H.

In this research study, doping of hydrogenated amorphous carbon films were attempted by incorporating Er through thermal evaporation of Er contained in metal-organic compound, $Er(TMHD)_3$ and $Er(acac)_3$, in a hydrocarbon flow discharge generated by unique DC saddle-field deposition system. Using these techniques, we can have better control on the Er incorporation and the a-C:H film properties to study the suitability of a-C:H as a host material for the 1.5μm light generation and amplification. We investigated different growth conditions to deposit a-C:H films with highest optical bandgap, utilized various doping techniques, and finely tuned evaporation conditions to produce controllable and homogeneous doping profile. We also explore the effect of deuteration of amorphous carbon (a-C:D) on the Er emission. The efficiency of 1.5μm light generation in Er-doped a-C:H and a-C:D films was characterized by photoluminescence spectroscopy (PL). The results of this project will add to the database of knowledge in this field.

This thesis is organized in the following format. In Chapter 2 and 3, the properties of a-C:H and metal-organic Er complex discussed, respectively. Chapter 4 focuses on the deposition system and deposition procedure and parameters used to grow Er-doped a-C:H films. Chapter 5 outlines experimental characterization techniques and brief principles are included. The characterization results and discussion of a-C:H(Er) and a-C:D(Er) are presented in Chapter 6. Finally, a general conclusion and future work are provided.

Chapter 2

Hydrogenated Amorphous Carbon (a-C:H)

2.1 Introduction

Amorphous carbon films (a-C:H) are frequently deposited by plasma enhanced chemical vapor processes (PECVD). This technology is very promising because of its high control of film quality, its easy integration in current micro-electronics technologies, its low cost, high efficiency and reproducibility. Recently, it has been shown that films have various optical and electrical properties [14, 15]. Then, as such films can be etched by oxygen plasma, they can be used for a great number of opto-electronic components (light source, detector, amplifier, waveguide, optical sensor and etc.). In this chapter, basic background information is provided, as well as the rationale behind choosing a-C:H as a host material for Er.

2.1 Various forms of carbon

Carbon, with $1s^2 2s^2 2p^2$ electron configuration in its ground state, has four L shell electrons, i.e., two in the 2s orbital and two in the 2p orbital. Under suitable conditions, these 2s and 2p atomic orbitals in the carbon atom can undergo three different hybridizations denoted as sp^3, sp^2, and sp^1.

Depending on the particular hybridization, carbon can form different structures with different geometries and mainly different fraction of sp^3 and sp^2 bonding in crystalline and non-crystalline forms (Table 2.1) [16]. Generally, only sp3 and sp2 sites are present in hydrogenated amorphous carbon (a-C:H) which contains a mixture of sp^3 and sp^2 bonded carbon and exhibits properties between those of diamond (100% sp^3 bonding) and graphite (100% sp^2 bonding). As seen in Table 2.1, the higher the concentration of sp^3 bonding and hydrogen content in a-C:H, the higher its bandgap.

2.2 Role of hydrogen

The hydrogen in a-C:H plays an important role in determining its properties. It not only passivates the dangling bonds to reduce the number of defect states near the mid gap, but also promotes sp^3 bonding, resulting in a-C:H with a high hydrogen concentration and larger band gap.

***Table 2.1**: Properties of various forms of carbon [16].*

	Density ($g.cm^{-3}$)	Hardness (GPa)	sp^3 %	Hydrogen %	Band gap (eV)
Diamond	3.515	100	100		5.5
Graphite	2.267	-	0		0
Evaporated a-C	1.9 - 2.0	2 - 5	< 5		0.4 - 0.7
Hard a-C:H	1.6 - 2.2	10 - 40	30 - 60	20 - 40	0.8 - 1.7
Soft a-C:H	0.9 - 1.6	< 5	50 - 80	40 - 65	1.6 - 4

2.3 Hydrogenated amorphous carbon

The growing interest in hydrogenated amorphous carbon films stems from its wide range of optical properties that result from the way its atomic orbitals are hybridized when making chemical bonds [17]. The unique properties of a-C:H depends primarily on the complex structure involving different bonding configurations and on the incorporation of hydrogen in the films. Hydrogen, being a terminator in the carbon network, plays a crucial role in determining the properties of the films. The structure of, and the incorporation of hydrogen in, a-C:H films are critically determined by the energy of the ionic species and the composition of the gas mixture in the deposition process. The ion energy can be changed by varying the deposition parameters. Therefore, it is feasible to obtain a-C:H films with a wide range of properties by adjusting the deposition parameters in the growth process. This flexibility in the opto-electronic properties of a-C:H suggests its potential suitability as a host material for Er. Specifically, a-C:H offers the following desirable properties [18]:

- Compatible with silicon and silica: Good adhesion to silicon-based materials allows convergence of photonic and electronic devices.
- Low optical absorption in the infrared spectral region of a-C:H: Optical absorption loss in 1.5 μm degrades photonics device in optical communication network.
- High optical quality film: High surface quality material is required for minimizing the light coupling losses.
- Conductivity from 5×10^{3} to 5×10^{5} $S.m^{-1}$ by doping with group III and V elements and tailorable optical gap in the 0.9 – 3.5 eV range: These

properties make a-C:H a viable material for realizing heterostructure, and potentially optoelectronic devices.

- Tailorable refractive index from 1.47 to 2.76: Waveguide-based applications.

All of these properties make a-C:H a suitable host material for Er to achieve our final goal: develop silicon-compatible material to generate light in the 1.5 μm region. In this project, a-C:H is prepared by DC saddle-field glow discharge deposition system, which provides quasi-independent control of ion energy and ion flux reaching the substrate, thereby enhancing the range of properties that the films can potentially attain.

Chapter 3
Metal-organic Erbium Complex

3.1 Introduction

Erbium is a rare earth element belonging to the group of the Lanthanides with atomic number 68. Erbium was first discovered in the Swedish town of Ytterby in 1842 by Carl Gustaf Mosander. Since the initial demonstration by Ennen et al. [2] in 1983 of light emission from Er-doped Si, seeking an alternative Er-doping method is always a hot topic in this research field. Evaporation of volatile organic lanthanide complexes, especially lanthanide β-diketonate complexes, are of particular interest for the deposition of lantahanide (e.g. erbium)-containing material. Previous attempts have included doping $Er(TMHD)_3$ in SRSO deposited by ECR-PECVD [19] and $Er(HFA)_3$*DME in a-Si:H deposited by PECVD [20]. Photoluminescence was demonstrated in both materials. In 2006, Zhao et al. [21] also showed 1.54μm Er^{3+} electroluminescence from an erbium-compound-doped OLED with $Er(acac)_3$ as a dopant in the electron transporting layer. In this research project, the goal was to incorporate erbium as an optically active center (Er^{3+}) through the use of metal-organic dopant sources. In this chapter, the rationale of using erbium β-diketonate complex as a dopant is addressed.

3.2 Erbium free-ion and crystal–field perturbation.

Erbium luminescence originates from the $4I_{13/2}$ to $4I_{15/2}$ transition in the $4f^{11}$ shell of the Er^{3+} ions. In the free-ion case, this transition is forbidden by the parity selection rule (Laporte rule), but are partially allowed in low symmetry sites by crystal field interactions (caused by the host) mixing odd- and even-parity wavefunctions and hence relaxing the dipole selection rules [22]. It is the magnitude of the crystal field that determines the degree of parity mixing, and it is the degree of parity mixing that controls the transition probability. Therefore, the transition probability can be changed by modifying the crystal field surrounding the Er atom.

Stark-splitting due to the crystal field of the host lifts degeneracy of the erbium 4f energy levels and give rise to different energy levels, which results in a broadening of the optical transitions. Fig. 3.1 shows the splitting of the $4f^{11}$ electronic energy levels of the Er^{3+} ion in a solid host. Because of the fact that the 5s and 5p shells shield the incomplete 4f shell, as a result, these energy levels are independent of the host material [22], so one can expect that energy levels of Er are almost the same as shown in Fig. 3.1. Erbium has become a technologically important ion since the transition from the first excited state to the ground state corresponds to $\lambda = 1.54$ μm, which coincides with the wavelength of maximum transmission in silica optical fibers, used widely in optical communication. One of the most successful optical amplifiers, Erbium-doped fiber amplifiers (EDFA), makes use of Er to realize gain in a region near 1.54 μm.

The Photoluminescence (PL) mechanism of Er^{3+} can be understand from in Fig. 3.1: when Er is excited to one of its higher excited states (e.g. second excited state in Fig. 3.1), it rapidly relaxes to first excited state via multi-phonon emission. This transition has typical lifetimes ranging from 1 ns to 100 ns. The transition from the first excited state to ground state is an exception to this case. Due to the large transition energy (0.8eV) phonon emission is unlikely, together with the parity selection rule, resulting radiative lifetimes up to ~ 10 ms depending on the host material, and leading to efficient emission at 1.54 μm. Due to the large difference between the lifetimes of these two states, most of Er ions stay in first excited state; hence optical gain can be realized by establishing a population inversion when pumped sufficiently.

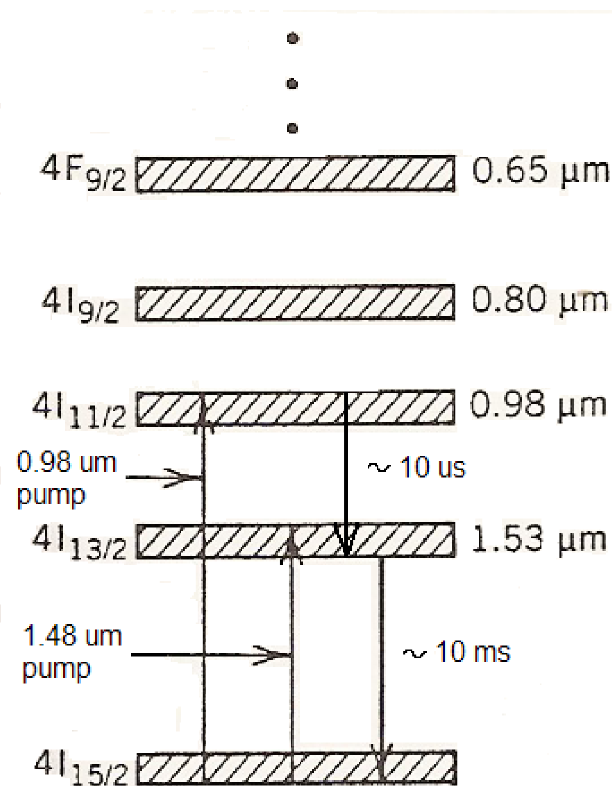

***Figure 3.1**: Schematic representation of the Stark-split Er^{3+} electronic energy levels, showing excitation at 0.98 and 1.48 um, followed by rapid non-radiative relaxation and emission at 1.54 μm.*

3.3 Erbium-containing β-diketonate complexe

Erbium contained metal-organic compounds were chosen as a dopant in the present work is because of the fact that it provides the following advantages:

(1) Optically active Er (Er-O)

Luminescence intensity is related to how efficiently the Er ion acts as an optically active center. It is well known that oxygen is often used to oxidize Er to be optically activated (triply charged). By increasing the oxygen content in the Er doped Czochralski (Cz) silicon sample, Priolo et al. demonstrated that this saturation in the luminescence intensity was caused by a lock of oxygen atoms, and also indicated that the nearest neighbor to Er in the Cz silicon sample is oxygen and that is the main reason for the Er ion to be an optically active center [23]. The magnitude of the crystal field around the Er atom is a function of the orientation and chemical nature of the ligands bound to the Er ion. As a result, it is the local chemical environment around the Er ion that is the largest factor in determining its optical activation. The larger electronegativity of oxygen results in a much stronger ligand field surrounding the Er ion in Er-O complexes compared to Er-Si complexes.

Tha major advantage of using Er contained metal-organics stemmed from the fact that the Er ions are in desired optically active bonding arrangement and the incorporation of organic ligands does not lead to an addition contamination. Beach et al. used MOCVD to deposit erbium-doped silicon using tris-1,1,1,5,5,5-hexafluoro-2.4-pentanedionato Erbium (III) [24]. The epitaxial quality was limited by the incorporation of fluorine, carbon, and oxygen into the films, with

the large organic ligands can give rise to a carbon concentration that is orders of magnitude larger than the erbium concentration. This much carbon can destroy the epitaxial growth of the film leaving useless carbon-rich amorphous layers. This will not be the case if the organic ligands are incorporated into the amorphous carbon film being used as a host material in this present study. However, the deposition process must be optimized such that the Er-O bonds do not break apart during its transport and after releasing the Er atom on the film surface.

(2) Elimination of Er-Er interactions

An additional factor which directly influences luminescence intensity is the density of optically active Er centers. Although high Er^{3+} concentration in the films can give rise in an increase of the effective excitation cross section of the Er ions, but often leads to the formation of cluster type Er compounds that reduce the Er lifetime due to energy transferring among Er ions, resulting in a net negative effect for the luminescent efficiency [25]. These problems can be solved by employing suitable Er precursors either containing bulky ligands or being encapsulated with proper material to prevent agglomeration and ensure the homogenous dispersion [26].

(3) Ligand-metal ion sensitization

Weissman described in a seminal paper the possibility of sensitizing lanthanide luminescence by transfer of the excitation energy from the surrounding ligands to the central metal ion (*antenna effect*) [27]. From the 1980s on a lot of attention has been paid to the luminescence of molecular lanthanide compounds, and especially to the β-diketonate complexes [28, 29]. By synthesizing lanthanide complexes it is possible to increase the absorption cross-section of Er ion. If the ligand contains a light-absorbing group, excitation energy is absorbed by this antenna and can be

transferred to the encapsulated Er ion. Three mechanisms have been proposed (Fig. 3.2) [30-32]:

Mechanism I. After an efficient intersystem crossing between the lowest singlet and triplet excited states of the ligand, energy transfer occurs from T_1 to a lower energy state (En) of the lanthanide ion:

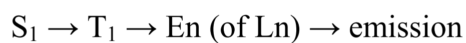

$S_1 \rightarrow T_1 \rightarrow$ En (of Ln) $\rightarrow$ emission

Mechanism II. There is a direct energy transfer from S, to a lower energy state (En) of the lanthanide ion:

$S_1 \rightarrow$ En (of Ln) $\rightarrow$ emission

Mechanism III. There is an energy transfer from S_1 to an upper intermediate level (Em) of the lanthanide ion, then back to T_1 to return finally to a lower energy level (En) of the lanthanide ion before emitting:

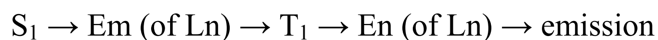

$S_1 \rightarrow$ Em (of Ln) $\rightarrow T_1 \rightarrow$ En (of Ln) $\rightarrow$ emission

In order to observe fluorescence from lanthanide ion under such indirect excitation, at least one *f-f* transition level of the ion should lie below the lowest triplet level of the ligand, otherwise the ligand-localized emission can be observed.

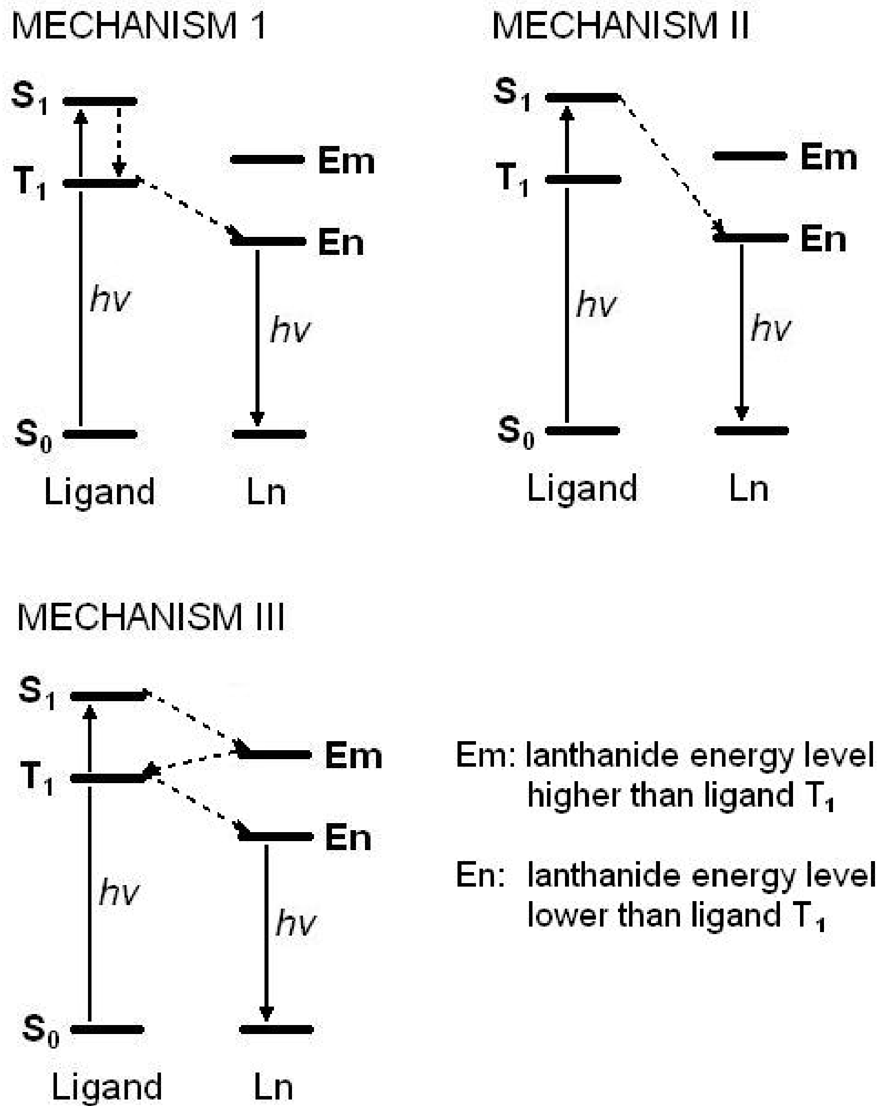

Figure 3.2: *Three different mechanisms for energy transfer in lanthanide complexes.*

(4) Low-temperature optically activated Er ion incorporation

Ion implantation is by far the most widely used method to incorporate Er into a Si-based host lattice. Although ion implantation is a nonequilibrium process which allows the introduction of high concentrations of Er, it results in a large amount of lattice damage. A high-temperature annealing is required to repair lattice damage and to optically activate the Er. In this project, the process of incorporating optically active Er complexes in the host without the need for additional high-temperature processing was attempted through the use of volatile metal-organic complex. The high

vapor pressure of the metal-organic compound allows its transport in the deposition chamber containing hydrocarbon gas.

The metal-organic compound Tris(2,2,6,6-tetramethy1-3-5-heptanedinoato) Erbium(III) ($Er(TMHD)_3$) was chosen. This metal-organic is a pink powder with a melting point of 168-171 ˚C and a boiling point of 290 ˚C. The Er^{3+} is located in an asymmetric octahedron of 6 oxygen which are linked in pairs to carbon chains (Fig. 3.3). The compound was obtained from Strem Chemicals, Inc. the chemical composition of this metal-organic is $Er(C_{11}H_{19}O_2)_3$ and it has an atomic weight of 717.08 amu. This particular metal-organic was selected for the following summarized reasons:

- It has a vapor pressure of 0.1mm Hg at 160 ˚C, and this vapor pressure makes it possible to deliver a controlled reactant stream with a mass flow delivery system.
- Er is in desired optically active bonding arrangement; the ligands are attached to the Er ion through two oxygen atoms, six in total (Fig. 3.3). No post annealing is required.
- Er is encapsulated with ligands. Er clustering can be avoided and higher doping levels can be achieved.
- Low effective Er excitation cross-section can be bypass through the *antenna effect* (ligand sensitization).
- The incorporation of this metal-organic compound does not introduce unwanted contamination in the host material.

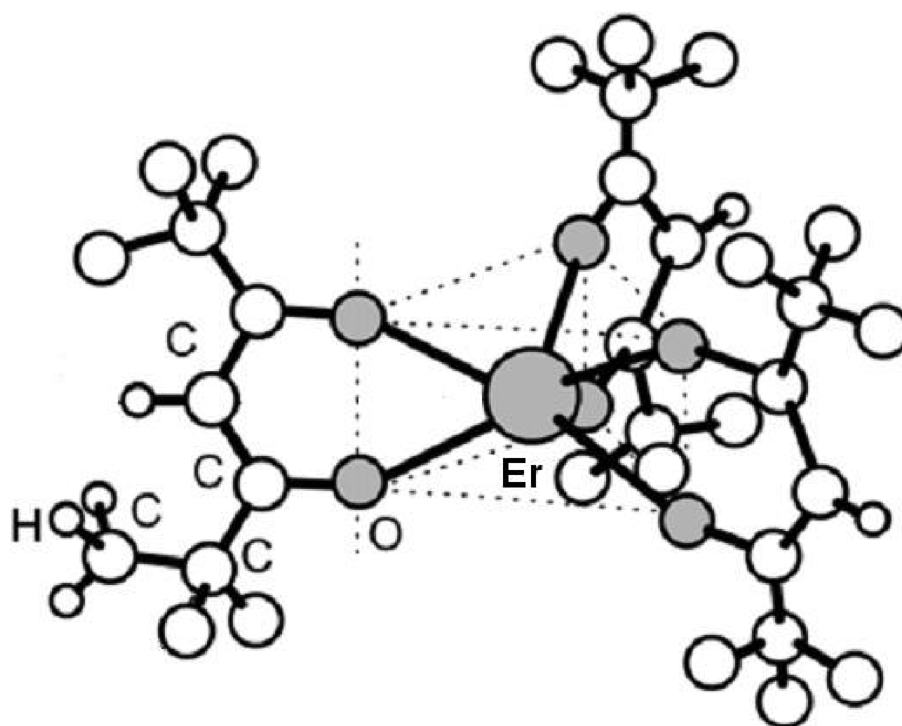

Figure 3.3: *Molecular structure of Tris(2,2,6,6-tetramethy1-3-5-heptanedinoato) Erbium(III) [33].*

Chapter 4

Sample Deposition

4.1 Introduction

Thin film deposition processes consist of three main steps: (1) production of the appropriate atomic, molecular, or ionic species, (2) their transport to the substrate through a medium, and (3) deposition on the substrate to form a solid film. When depositing a thin film, one has to choose appropriate conditions over a broad range of parameters involved in the above three steps, and a method of deposition to achieve a film with desirable properties. This chapter describes first the traditional deposition methods used to deposit amorphous semiconducting thin films, and then the DC saddle-field (DCSF) glow discharge deposition technique which was used in the growth of films for the present study. In addition to conventional DCSF deposition system, a thermal evaporator is integrated onto the deposition system to facilitate the Er doping. The last section of this chapter gives details of sample preparation and relevant deposition parameters.

4.2 Conventional thin film deposition techniques

4.2.1 Chemical vapor deposition

In the chemical vapor deposition process (CVD), a solid-phase reactant product (thin film) is deposited on a heated substrate surface from appropriate reactant vapors

by a chemical reaction involving direct elemental combination. The substrate material, substrate temperature, composition of the reactant gas mixture, flow rate, and total pressure of the gas can be varied to deposit materials with different properties. In chemical vapor deposition, gaseous reactants are admitted into a reactor as shown in Fig. 4.1, and the following type of chemical reaction occurs between gaseous reactants near or at the heated substrate surface.

Gaseous reactants → Solid material + Gaseous products

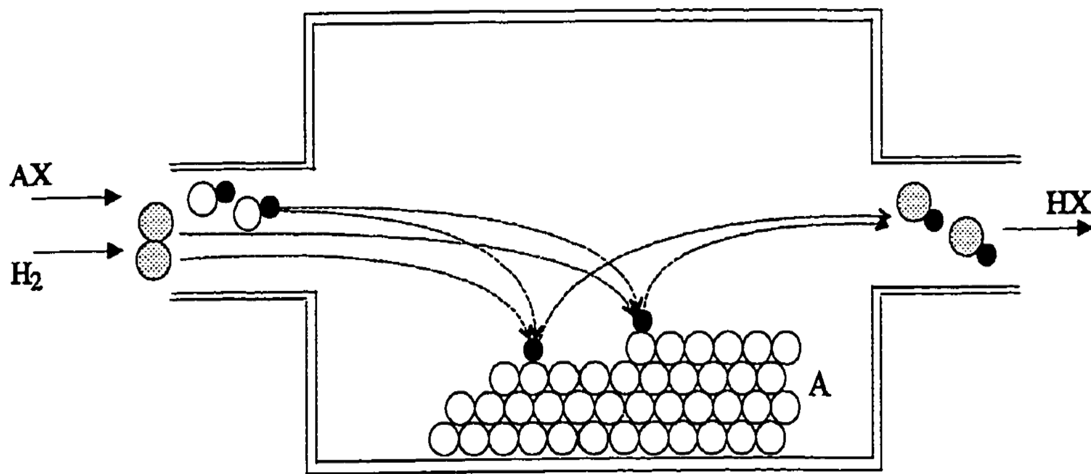

Figure 4.1: *A common implementation of CVD (AX, H2, HX – gases, A – solid material) [29].*

There are some drawbacks to CVD, since the process often requires high temperatures for a chemical reaction to happen. In some cases, the temperature necessary to achieve acceptable deposition rates may be so high as to lead to diffusion, alloying, or chemical reactions on the substrate surface. This limitation of CVD can be overcome if an electric discharge is created in the reactant gases to produce a significant number of free radicals, which will be much more reactive at lower temperature. The latter process is known as plasma enhanced chemical vapor

deposition (PECVD). Depending on the form of excitation used to create the discharge, there are two distinct types of discharge – DC and RF.

4.2.2 DC glow discharge

The term DC glow discharge normally refers to the DC diode glow discharge configuration. When a sufficiently high DC voltage is applied between the two electrodes in a gaseous medium at reduced pressure, the atoms and molecules in the medium will break down, creating electron-ion pairs and letting a current flow. A typical current-voltage characteristic of a DC glow discharge is illustrated in Fig. 4.2. At low voltages, the discharge current is due to the primary electrons and ions produced by external sources such as cosmic radiation. As the voltage is increased, when all the charges have reached the electrodes, the current becomes independent of voltage. This is referred to as the saturation regime. Beyond the saturation regime, the current starts to increase with increasing voltage in the Townsend regime. In this latter regime some primary electrons gain enough energy to ionize the gas species, producing positive ions and additional electrons. If the voltage across the tube carrying a Townsend discharge is increased, the current starts to increase sharply, perhaps by several orders of magnitude: this is referred to as breakdown. At this point, cathode bombardment and secondary electron emission occur as the positive ions gain sufficient energy to travel to the cathode and promote secondary emission and a positive feedback occurs due to the regeneration of electrons and the discharge is self-sustained. As the current is increased further, the voltage across the tube decreases until V_G, the voltage required to sustain the discharge. At the onset of the normal glow regime, a luminous glow starts to grow at the cathode surface. No voltage increase is required as the current continues to increase, since the increase in

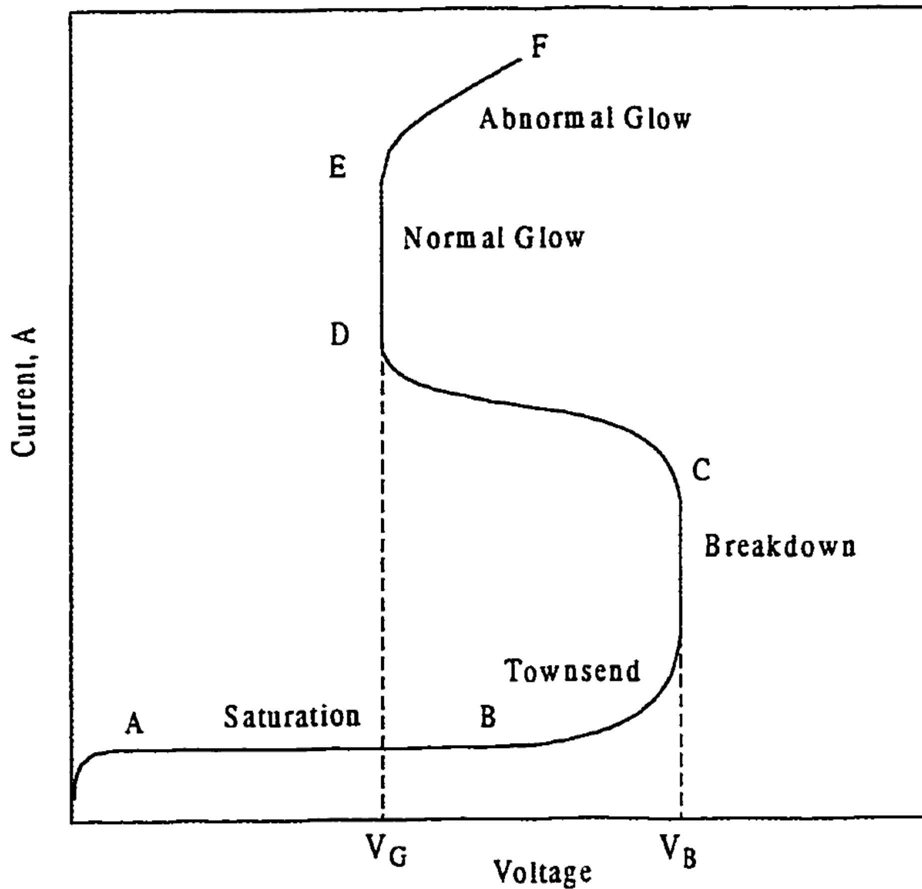

Figure 4.2: *Cureent-voltage characteristics in a DC glow discharge [35].*

current does not change the current density but only the cross-sectional area of the discharge. After the discharge entirely covers the cathode surface, any further increase in the discharge current results in an increase in the current density, hence requiring an increase in the discharge voltage. This last condition is known as abnormal glow discharge. To obtain uniformity in depositing thin films, the abnormal glow regime is used to for the deposition.

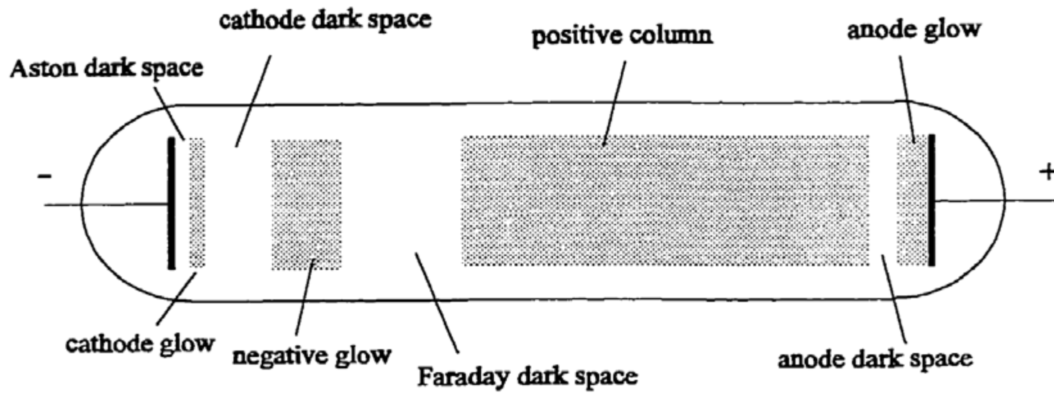

Figure 4.3: *Luminous zones and dark spaces in a DC glow discharge [36].*

A low pressure glow discharge plasma contains alternate dark and bright luminous layers, as described in Fig. 4.3. All of the luminous zones illustrated in Fig. 4.3 are observed only when the inter-electrode separation is large compared to the size of the electrodes. In practical glow discharge systems used for thin film deposition, the inter-electrode separation needs to be comparable to the size of the electrode. When the electrode separation in Fig. 4.3 is decreased, the positive column shrinks. This process continues until the positive column and also all the other zones disappear except the negative glow, cathode dark space, and anode dark space. The potential relative to the cathode increases linearly in the cathode dark space (also called the cathode sheath), starting from the negative cathode potential V_C, and reaches a constant plasma potential V_P that is maintained in the negative glow regime, and then drops to zero in the anode dark space (also called the anode sheath). The potential distribution for such a case is shown schematically in Fig. 4.4. Most analytical glow discharge sources are designed so that the inter-electrode separation is a few times the length of the cathode dark space.

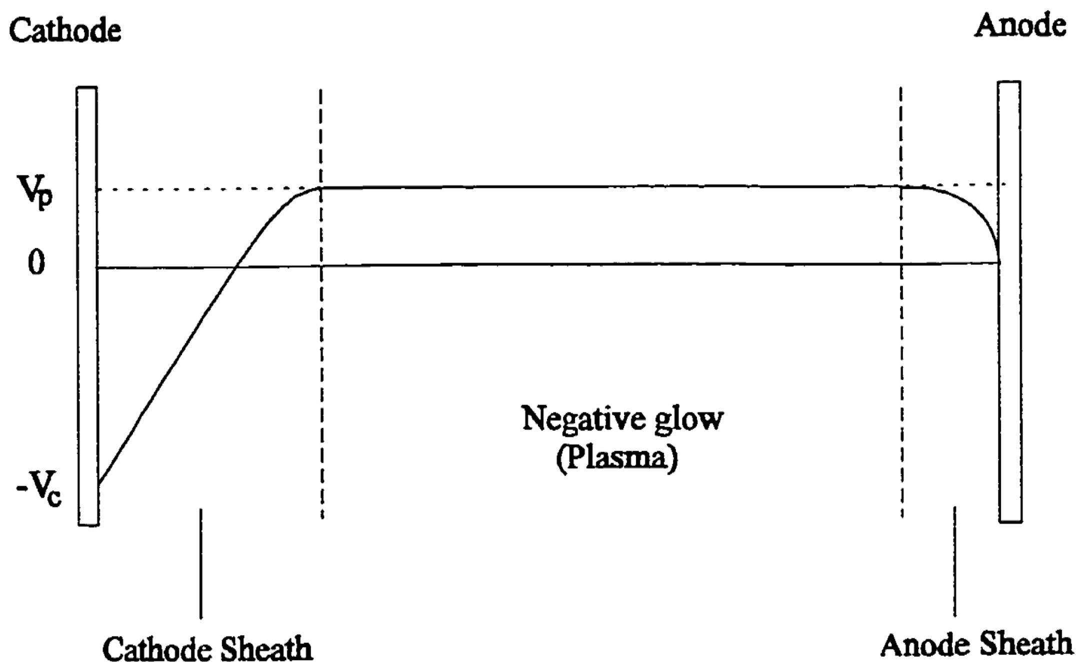

Figure 4.4: *The potential distribution in a DC glow discharge (V_P - plasma potential, V_C – cathode potential) [37].*

The negative glow region in Fig. 4.4 contains a partially ionized gas with equal numbers of positive and negative charges, in addition to the neutral species, and is characterized as a plasma. In this region, gas molecules undergo inelastic collisions with energetic electrons, resulting in ionization, dissociation, or excitation [37]. The relaxation of excited molecules back towards the ground state is accompanied by emission of ultraviolet or visible photons, which result in the glow in the negative glow region (plasma).

The entire voltage drop in the glow discharge occurs at the boundaries of the negative glow (in the sheath regions, Fig. 4.4). The behavior of these regions is important to sustain the plasma. For instance, due to the large voltage drop in the cathode sheath, the ions are accelerated towards the cathode where the bombardment

occurs, resulting in secondary electron emission form the cathode. The same voltage drop in the cathode sheath accelerates these secondary electrons towards the negative glow, where they then undergo inelastic collisions to produce ions and radicals. The sheath region is mostly dark, since the secondary electrons undergo collisions with the neutral gas molecules only at some distance away from the cathode, corresponding to their mean free paths. The voltage drop in the anode sheath is relatively smaller. The opposite electric field repels some of the electrons to control the electron flow to match the electron current required by the external circuit.

4.2.3 RF glow discharge

The design of the electrode configuration for RF glow discharges is much the same as for DC glow discharges, but the electrodes are powered by an AC power supply. When the polarity of the electrodes is alternated, the mechanism of glow discharge generation is dependent on the frequency of the alternation. At low frequencies, the mechanism is simply the same as that of DC glow discharge of alternate polarity. However, as the frequency increases, the motion of ions no longer can follow the changes in the field polarity. A common operating frequency for RF glow discharge deposition is 13.56 MHz. At this frequency, due to the large mass difference between electrons and ions, only electrons can follow the variations in the applied field. Therefore, the plasma can be described as an electron gas which moves back and forth in a sea of relatively stationary ions. As the electron cloud approaches one electrode, the ions are exposed to the other electrode forming a positive sheath where the most of the voltage drop occurs. In the sheath region, the ions are accelerated and bombard the electrodes.

Since the oscillating electrons in an RF plasma do not reach the electrodes and no real current flows through the circuit in contrast to the DC case, the RF glow discharge does not require conducting electrodes in contact with the plasma. The production of the plasma is more efficient in an RF glow discharge than in a DC glow discharge, since the ionization is more efficient as the electrons gain higher energies as they follow oscillatory paths between the electrodes. On the other hand, RF systems can generally maintain high deposition rates with relatively low plasma potentials. For these reasons amongst others, RF method is often chosen over the DC glow discharge for PECVD. Nonetheless, the simplicity of the DC system and potential versatility continue to give it significant appeal and warrants further research.

4.3 DC saddle-field glow discharge system

The DC saddle-field glow discharge system has previously been proposed as an improvement over the DC diode for PECVD [38]. A combination of the positive attributes of the DC and RF glow discharge techniques is employed in the DC saddle-field glow discharge technique. The concept of using a saddle-field cavity as a high energy ion source goes back to the 1960's [39]. The saddle-field ion source is based on the concept of and electrostatic, charged-particle oscillator, where the particles of one sign (electrons) are confined to a limited range solely by means of electrostatic field, and are made to traverse long oscillatory paths. The saddle-field glow discharge deposition system which was employed to deposit a-C:H films for this study was designed and patented at the University of Toronto. The main components

of the saddle field system are a deposition chamber, a DC power supply, a vacuum pumping system, and a gas mixing and storage system (Fig. 4.5).

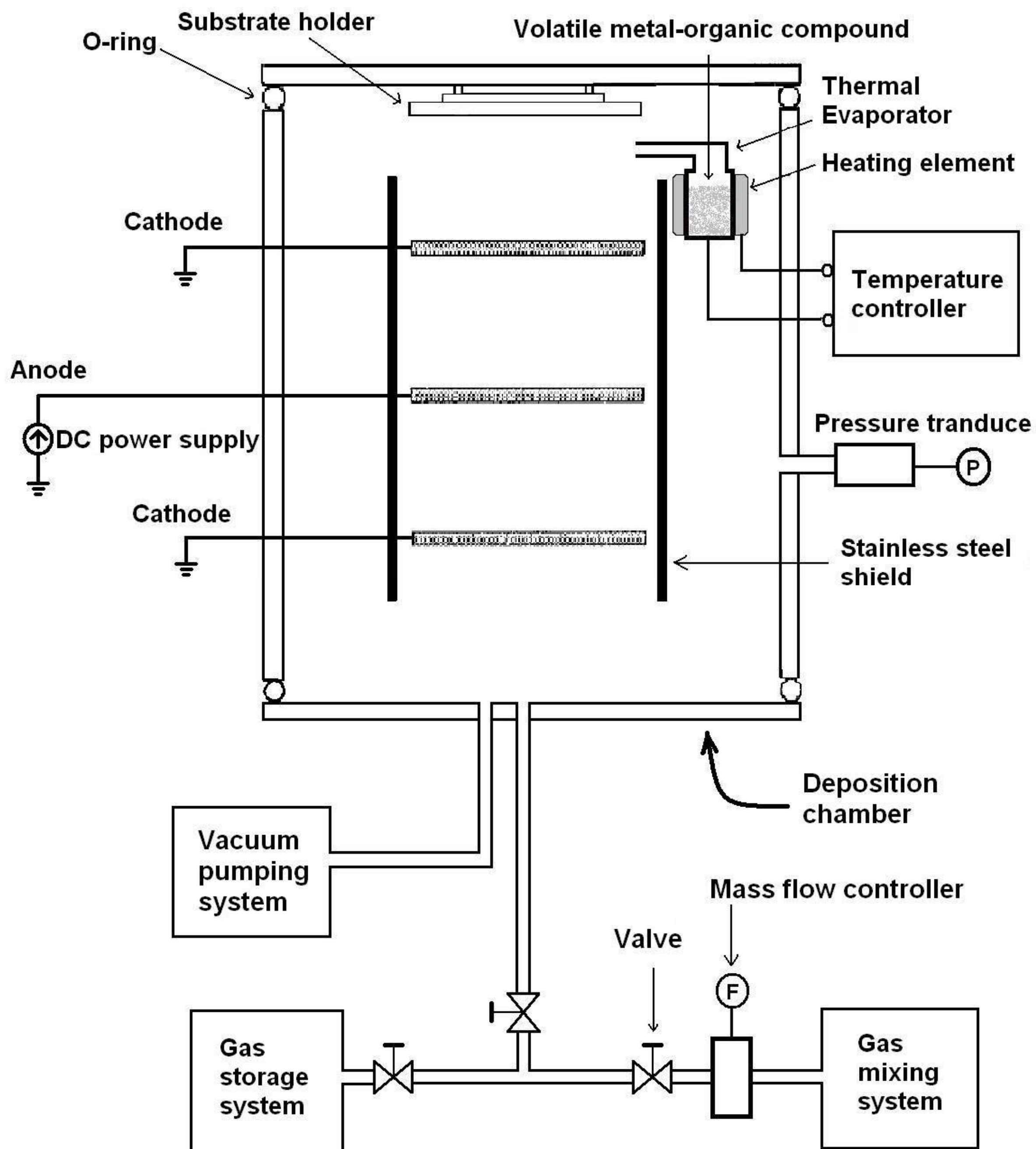

Figure 4.5: *A schematic diagram of the modified DC saddle-field glow discharge deposition.*

The saddle-field chamber contains a positively charged mesh anode located symmetrically between two parallel electrically grounded mesh cathodes and two outer electrodes as shown in Fig. 4.5 [40, 41]. The chamber and the electrodes are made of stainless steel. The chamber is 25 cm in diameter and 30 cm in length, and the electrodes are 15 cm in diameter. A cylindrical shield made of stained-less steel surrounds three electrodes, and laterally confines the glow discharge to ensure an efficient deposition.

When a positive voltage is applied to the central anode, an electrostatic field is created between the anode and the cathode. This electrostatic field traps the electrons between the anode and the two cathodes. The electrons are accelerated through the mesh anode and continue towards the cathodes; before they reach the cathodes, the electrons are attracted back towards the positive anode. This causes the electrons to follow a very long oscillatory path which passes back and forth many times through the mesh anode in the region between the two cathodes, before they are eventually collected by the anode. The electron mean-free path can, therefore, be much longer than the inter-electrode spacing [42]. If a gas is present in the chamber, these oscillating electrons provide an efficient means of ionizing the gas to create a large number of ions, radicals, and additional free electrons. The electrostatic field existing between the anode and the cathode also provides the energy to accelerate positive ions away from the anode towards the cathode; a significant number of the ions pass through the semitransparent mesh cathode towards the substrate.

The vacuum pumping system consists of a Balzers TPU 180H turbo pump backed by an Edwards mechanical pump and a CTI CT-100 cry pump. A Varian

980-1200 DC power supply is used to provide a constant current to maintain the discharge.

The saddle-field glow discharge source is unique in the way that it combines the benefits of DC and RF glow discharge systems; it uses a simple DC power supply to control the discharge as in the DC glow discharge while allowing for electron paths that are considerably longer than the inter-electrode spacing as in the RF glow discharge. The ability to control the substrate bias individually is a advantage over the other methods employed in thin film deposition. Due to this ability to control the substrate bias, it is possible to control the energy and the number of ions which reach the substrate per second from the plasma and hence vary the structure of the deposited films. A study of these possible deposition parameters are given in reference [43].

4.4 Thermal evaporator assembly

In this research, the method of incorporating Er into films utilizes the technique which is analogous to that of metal-organic chemical vapor deposition (MOVCD). Instead of using gaseous reactants in the case of PECVD, volatile metal-organic compound (solid or liquid) containing the required chemical element is sublimed, and then introduced into the reaction chamber. The advantages of using technique for the Er incorporation are listed in section 3.3. As seen in Fig. 4.5, the thermal evaporator assembly consists of a stained-less cylindrical reservoir containing the metal-organic compound, a band heater, a gaseous guiding tube and a PID temperature controller providing required temperature to the metal-organic compound. The surface

temperature sensor is attached to the bottom of the reservoir. The volume of the reservoir is 5 cm^3 which is equivalent to 1 g of $Er(TMHD)_3$.

As the sublimated metal-organic compound diffuses to the surface of the substrate, it encounters two unwanted processes, the condensation/accumulation and the dissociation. The condensation/accumulation occurs when the sublimed metal-organic compound contacts a cold surface before it reaches to the surface of the film. The dissociation is associated with fact that the organic cage can be broke apart by the collision with the energetic ion in the glow discharge, making Er is no longer optically activated (destroying its triply charged state), and causing a higher likelihood of clustering, therefore ultimately resulting in reduced photoluminescence (see section 3.3). To avoid these problems, the guiding tube is taped with the aluminum foil to improve the heat transfer from the heater, and the thermal evaporator is placed at the nearest position to the substrate without disturbing the glow discharge. This evaporator was 8 cm away from the edge of the substrate holder.

The Er content in the film directly depends on the position of the Er reservoir in the PECVD growth of Er doped a-C:H form gas mixtures of methane and $Er(TMHD)_3$. Vaclav et al. has demonstrated that the highest concentration of Er (8.74 mol%) in the carbon films was observed when the reservoir was located in the position one (1. Erbium tris in Fig. 4.6). When the reservoir was in the position two (2. Erbium tris in Fig. 4.6), the concentration of Er in the carbon films was usually lower (up to 0.02 mol%) [44].

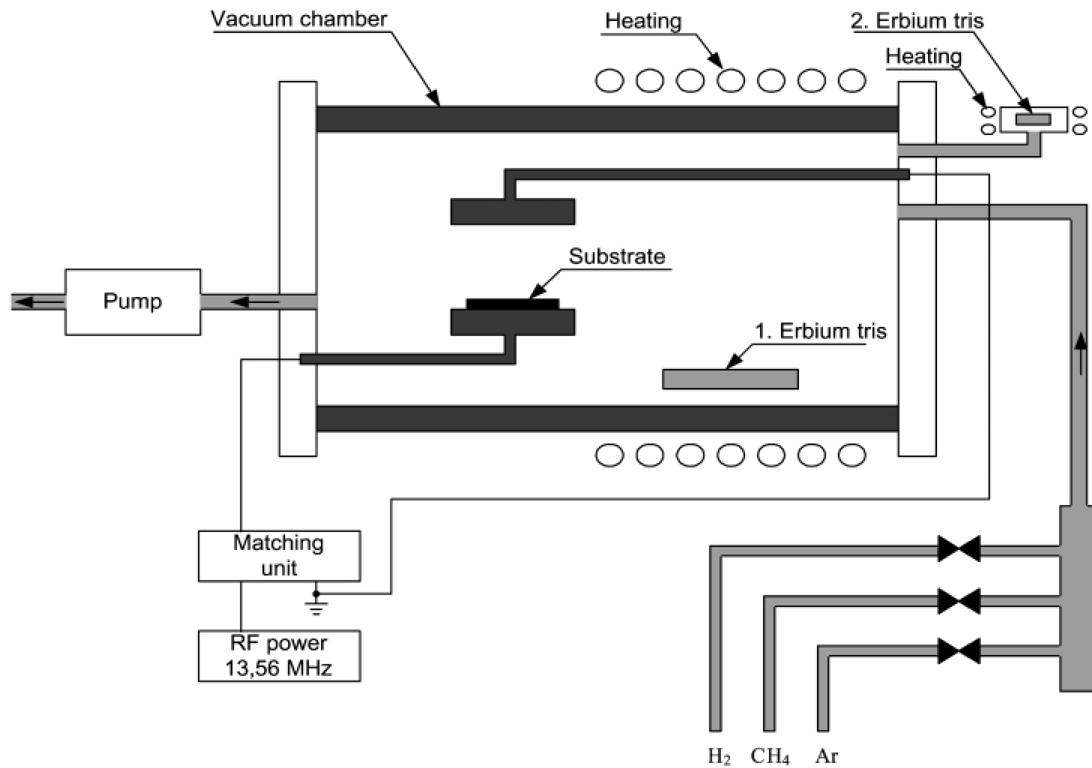

Figure 4.6: *The PACVD device for the deposition of carbon layers from methane and erbium metal-organic [44].*

4.5 Substrate and chamber preparation

Crystalline Si with <100> orientation, resistivity of about 10-20 Ω-cm and thickness of 600 μm, and insulating fused silica substrates with thickness of 1 mm were used as substrates for depositing our films. Since chemical bonding forces extend only a few tenths of a nanometer, only one monolayer of poorly bonded contaminant can be sufficient to prevent bonding of the depositing film to the substrate, causing poor adhesion between the film and the substrate. Also, contaminants can affect the structure and opto-electronic properties of the film. Contaminants, largely water and oil, come mainly from the atmosphere and handling;

they can be removed with degreasing solvents such as isopropyl and acetone. The substrates for our film depositions were cleaned ultrasonically in isopropyl and acetone for 15 minutes in each solvent, and were finally washed with deionized water and blow-dried.

The deposition chamber was prepared as follows. The grids, substrate holders, nuts and washers were immersed in a heated solution of sodium hydroxide, scrubbed with wire brushes, polished with silicon carbide sand paper, rinsed with deionized water and dried with dry compressed air. After cleaning they were place inside an oven for approximately 4 hours at a temperature of 150 ˚C and then mounted inside the deposition chamber. The mixing bottles, pipes and chamber were evacuated approximately 3 hours before Argon discharge cleaning by setting the turbo pump to maximum speed and opening all the valves that interconnect the system. The argon discharge cleaning was done by striking the Argon plasma with 200 mA and ~ 1 kV. The energetic Ar ion in the plasma can sputter away any residual contaminations, on the parts inside the chamber, left from cleaning and transporting, and to provide a stable plasma condition during the deposition. The Argon cleaning before a deposition consists of the following steps:

1. Strike the Ar discharge for 2 hours.
2. Bring the pressure of the chamber to atmosphere and load the substrates onto the substrate holder (this has to be done in 5 minutes).
3. Evacuate the chamber for 2 hours.
4. Strike the Ar discharge until the plasma is stable (~ 5 minuets).
5. Evacuate the chamber for 12 hours before the deposition.

The substrates were mounted on the substrate holder using screws and small stainless steel clamps. The base pressure of 2×10^{-6} mbar was achieved after 8 hours of pumping.

4.6 Deposition procedure and deposition parameters

Before performing a deposition, one should make sure the pressure of the chamber is at 2×10^{-6} mbar with all the valves opened that interconnect the system, the substrate holder is grounded, and the potential of the shield surrounding the electrodes is floating. When performing a deposition, the first step was to establish a constant substrate temperature by activating the substrate temperature controller. The required gas was delivered to the deposition chamber at a constant flow rate. Next, the turbo pump controller was activated to maintain a constant deposition pressure inside the chamber, and then the evaporator for the Er doping is heated up and kept constant at a predetermined temperature throughout the deposition. In this research, the reservoir temperature used for $Er(TMHD)_3$ is in the range of 145 ˚C to 165 ˚C, and 90 ˚C to 160 ˚C for $Er(acac)_3$. To start growing the film, the DC power supply was turned on and adjusted to ignite the glow discharge and provide a constant discharge current. The gas mixture was broken down in the plasma and film growth occurred. After the film was allowed to grow for a predetermined amount of time, the deposition was stopped by turning off the DC power supply, and the heater for the evaporator and for the substrate holder. Once the sample had cooled down to room temperature, it could be taken out of the deposition chamber. The sequence of these operations can be seen

clearly in Fig. 4.7. When the desired substrate temperature was reached the methane flow was turned on at time $t = t_1$. Simultaneously the evaporator was heated and reached its final temperature at t_3 ($t_3 - t_1$ = 12 minutes). The DC power for the glow discharge was switched on at t_2 ($t_2 - t_1$ = 10 minutes). The system was turned down after the time t_4, first the evaporator and then the DC power (with a little delay), the methane flow and the substrate heater. The deposition time is defined as time when the DC power is on.

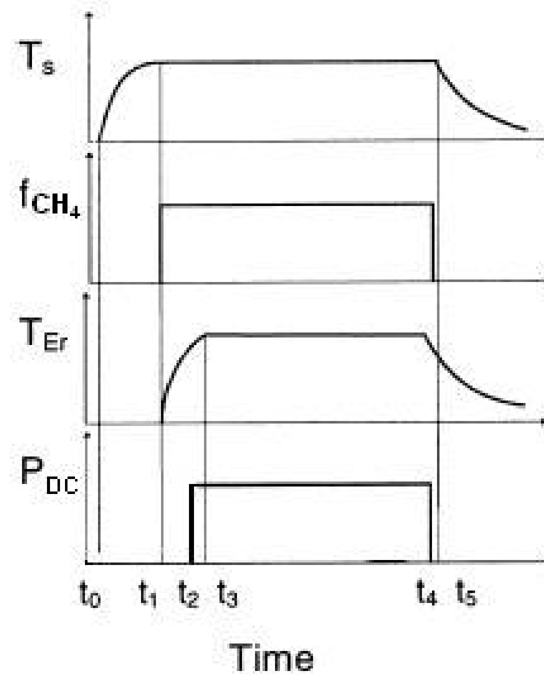

Figure 4.7: *The time sequence of experimental actions. The terms t_0 to t_5 are explained in the text, as Ts being the substrate temperature, f_{CH_4} being the methane flow, T_{Er} being the evaporator temperature, and P_{DC} being the DC power of the system.*

The first set of undoped a-C:H aimed to establish a suitable deposition condition that produce a diamond-like carbon with high optical quality (high bandgap and excellent surface quality). High optical transmission in the visible region is required

for luminescence materials to obtain the effective emission [45]. Based on the previous study on deposition of a-C:H prepared DCSF glow discharge deposition system [43], we were able to deposit the diamond-like carbon film by varying the substrate temperature and the anode current (try and error method). The highest bandgap of 2.8 eV in the undoped a-C:H films was observed when the following deposition conditions was applied:

Table 4.1: *Deposition parameters for the diamond-like carbon film.*

***Parameter*s**	***Settings***
Substrate temperature	30 - 60 ˚C
Deposition pressure	50 mTorr
Flow rate	5 sccm
Anode current	17 mA

The Tauc method used to compute the optical bandgap will be discussed in section 5.3 and the Tauc plot for the sample with the highest bandgap can be found in Fig. 5.3. The deposition pressure of 50 mTorr and the flow rate of 5 sccem were chosen for suppressing gas phase reactions that produce undesirable growth precursors, and thus to limit the probability of polymerization of methane [43]. It has been shown that the optical bandgap of the a-C:H films decreases with increasing substrate temperature [46-48], hence the substrate remained unheated for all of the Er-doped samples, however, the temperature of unheated substrate during the deposition varied from 30 ˚C to as high as 60 ˚C. The anode current was unable to increase beyond 17 mA with a stable plasma condition during the deposition.

Once the deposition condition for diamond-like carbon film was established, the next goal was to achieve high concentration Er doping and to produce a homogenous Er depth profile in the Er doped a-C:H films. Two sets of the Er doped a-C:H films were prepared by employing $Er(acac)_3$ and $Er(TMHD)_3$ precursors, respectively. Table 4.2 lists the deposition parameters associated with the films deposited using $Er(acac)_3$, and Table 4.3 contains that of the films deposited using $Er(TMHD)_3$. The substrate was grounded and not heated, and the deposition time was 1 hour and forty-five minutes for all samples. The films in Table 4.2 were used o study the effects of the evaporator temperature (B1 – B6), the deposition pressure (B1, B7 and B8), the flow rate (B1 and B9), and the anode current (B1 and B10) on the Er evaporation rate. For this set of samples, the Er luminescence was investigated by photoluminescence spectroscopy (PL). Only B1 and B2 were subjected to time-of-flight secondary ion mass spectroscopy (ToF-SIMS) measurement for the atomic and molecular composition and depth profile.

Table 4.2*: Deposition parameters for the set of ten Er doped a-C:H films deposited using the gas mixture (methane + $Er(acac)_3$).*

Film	***Evaporator Temperature (℃)***	***Deposition Pressure (mTorr)***	***Flow rate (sccm)***	***Anode current (mA)***	***Amount of $Er(acac)_3$ loaded (mg)***
B1	112-115	50	5	15	21
B2	128-130	50	5	15	20
B3	142-145	50	5	15	21
B4	158-160	50	5	15	20
B5	98-100	50	5	15	20

B6	88-90	50	5	15	21
B7	112-115	150	5	15	22
B8	112-115	20	5	15	19
B9	112-115	50	20	15	20
B10	112-115	50	5	5	21

The only variables in the deposition parameters that used to prepared second set of Er doped a-C:H films was the evaporator temperature and the amount of Er(TMHD)$_3$ loaded, while all other parameters were all the same (Table 4.1). Seven samples were prepared, as listed in Table 4.3.

***Table 4.3**: Deposition parameters for the set of seven Er doped a-C:H films deposited using the gas mixture (methane + Er(TMHD)$_3$).*

Film	***Evaporator Temperature (℃)***	***Amount of Er(TMHD)$_3$ loaded (mg)***
E1	23-133	26
E2	129-134	41
E3	132-137	69
E4	144-145	175
E5	160-161	504
E6	160-161	787
E7	160-161	860

For this set of samples, the Er luminescence was analyzed by PL. ToF-SIMS was used to detect the presence of the Er element. The samples (E2, E4, E5, E6 and E7) were subjected to X-ray photoelectron spectroscopy (XPS) for the depth profile studies and the atomic concentration of Er, C, Si, and O. Lastly, E3, E4, and E5 were thermal annealed at 100, 200, 300, and 400 ˚C in an H_2 environment.

It has been shown in the later section that the weak Er luminescence from the Er-doped a-C:H films, suggesting a competitive optical quenching mechanism, was originated from the coupling of the excited state of the Er^{3+} ion with high frequency vibrations of CH and OH groups in the host material. To support this hypothesis, the $Er(THHD)_3$ was dissolved/embedded in C-H free environments (deuterated methanol and KBr) to show the enhancement in the Er emission. As a result, it proved worthwhile to investigate the Er PL in a-C:D. The details of preparation for the deuteration are included in the next section.

For the last deposition, a strip (10 × 1.5 cm) of Er doped deuterated amorphous carbon was prepared using the gas mixture (CD_4 + $Er(TMHD)_3$). The deuterated methane (CD_4) was obtained form Sigma-Aldrich (product # 490245). The amount of $Er(TMHD)_3$ loaded was 631 mg and the evaporator temperature was kept at 145 during the film growth. Other deposition parameters are listed in Table 4.1. The PL and XPS analysis were performed on four spots. The spots were 15, 13, 10, and 7 cm away from the Er reservoir. The binding energy spectra obtained from XPS analysis were used to study the chemical environment around Er ions. The Er luminescence spectra at different spots were compared and correlated with their Er concentrations.

4.7 Preparation of $Er(TMHD)_3$ in KBr and organic solvents

In order to be useful for applications, the light-emitting compound has to be embedded into a matrix. The luminescence properties of $Er(TMHD)_3$ were also studied in the solid state (as diluted material in KBr), or as solutions in methanol and in deuterated methanol solvents. The luminescence spectra of 0.5, 1, 2, 5, and 10 mol% of $Er(TMHD)_3$ diluted in KBr were compared with that of 2 mol% in methanol. On the other hand, 1.1 mol% of $Er(TMHD)_3$ in methanol were compared with that in deuterated methanol. The deuterated methanol was obtatined form Sigma-Aldrich (product # 151947).

Chapter 5

Experimental Characterization Techniques

5.1 Introduction

The study of the potential suitability of a-C:H as a host for 1.54 μm light emitting applications, is one of the main objectives of the present work. A number of diagnostic techniques were chosen to provide a set of information which proved the feasibility of the modified deposition techniques. These diagnostic studies of Er doped a-C:H films not only characterize the material but also characterize the deposition process. Thickness measurements, ultraviolet and visible, X-ray photoelectron, time-of-fight secondary ion mass, and photoluminescence spectroscopies were used to reveal the Er luminescence and the optical properties of Er doped a-C:H thin films. This chapter provides the details of the above methods and explains some of the theory underlying each method. The analysis of the measurements for the samples using these techniques will be presented in the following chapters.

5.2 Film thickness measurement

The thickness of our thim film sample is typically a fraction of a micrometer. In order to measure such small thicknesses, special equipment such as a Tencor Alpha-step thin film profilometer has to be used. A profilometer has a diamond tipped stylus. When the stylus moves across a step, the height of the step can be obtained by measuring the deflection of the stylus. By knowing the height of the step, as the one shown in Fig. 5.1, one can determine the thickness of a thin film.

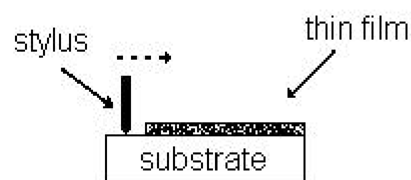

Figure 5.1: *The thickness of a thin film can be measured using a profilometer.*

To create such a step, one can use a stained-less steel clamp to cover up part of the substrate before the deposition. As a result, during the deposition, the film will not grow on the area covered by the clamp. When the deposition is finished, the clamp can be removed and a step will be created. The thickness of the sample can then be determined using a profilometer. Fig. 5.2 summarizes the procedures used to create a step.

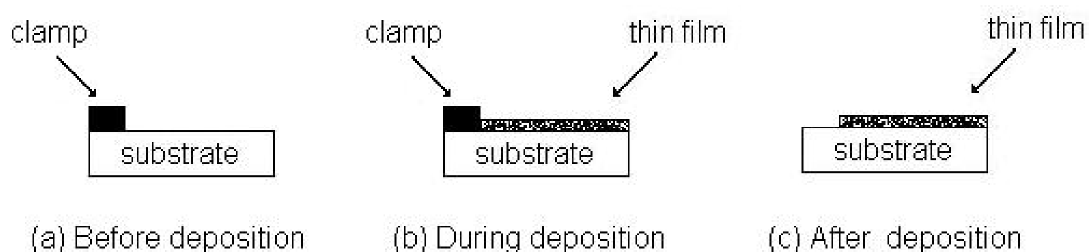

Figure 5.2: *The procedures to create a step.*

5.3 Ultraviolet and visible spectroscopy

In contrast to crystalline semiconductors, no sharp absorption edge is present in amorphous semiconductors, due to the tail states which originate from the disorder. It has been suggested that an empirical gap E_g which characterizes the absorption can be defined in terms of an extrapolation of bands of extended states [49]. The optical absorption in amorphous materials may be modeled by the Tauc formula

$$\sqrt{\alpha E} = B(E - E_g) \tag{5.1}$$

where α and E are the absorption coefficient and the photon energy respectively, and B is a constant. The above equation is characteristic of the parabolic band edges found in crystalline materials, but is often used to determine an optical band gap parameter E_g which characterizes the absorption in amorphous semiconductors [50].

A simple procedure based on Eq. 5.1 can be used to extract E_g from data on the variation of α with E which can be deduced from transmittance and reflectance measurements of ultraviolet and visible radiation. It can be shown that the relationship of the absorption coefficient α to the transmittance T and reflectance R can be expressed as

$$T = (1 - R)\exp(-\alpha d) \tag{5.2}$$

which is valid in the spectral region of fundamental absorption [51]; d is the thickness of the film. By combining Eq. 3.1 and 3.2, one obtains

$$\sqrt{\alpha d E} = \sqrt{\ln\left(\frac{1-R}{T}\right)E} = B\sqrt{d}\,(E - E_g) \qquad (5.3)$$

It is then possible to obtain E_g by extrapolation of the linear part of the graph of $\sqrt{\ln\left(\frac{1-R}{T}\right)E}$ versus E (Fig. 5.3).

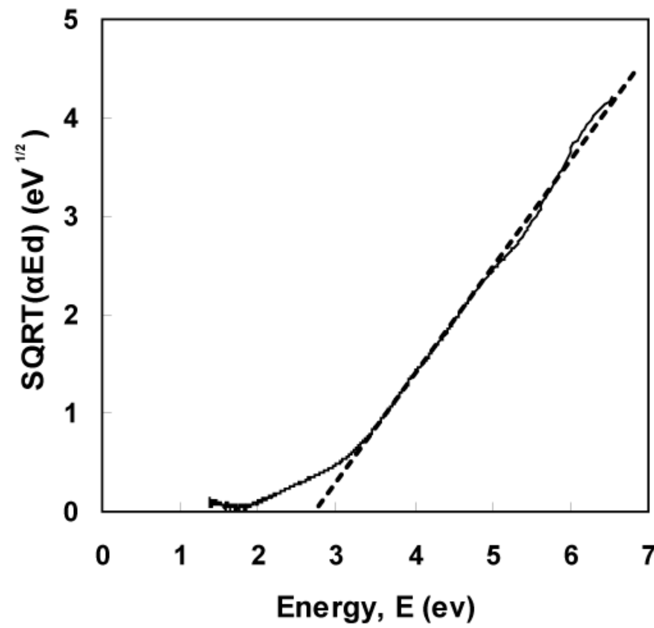

Figure 5.3: *Tauc plot for an undpoed a-C:H sample in the present study. The dashed line shows that the extrapolated Tauc gap is 2.8 eV.*

The transmission and reflection of a-C:H thin films on quartz substrates were measured in the range of 190 - 900 nm using a Pekin Elmer ultraviolet/visible Lambda 18 spectrometer.

5.4 X-ray photoelectron spectroscopy

X-ray photoelectron spectroscopy (XPS) is one of the major surface analytical techniques based on emission and energy analysis of low energy electrons (generally in the range of 20- 400 eV). The electrons are emitted from the sample as a result of the photoemission process when the sample is irradiated with soft X-rays. The spectrum consists of the number of detected electrons per energy interval as a function of the kinetic energy of the electrons. The electron emission processes in XPS is shown schematically in Fig. 5.4.

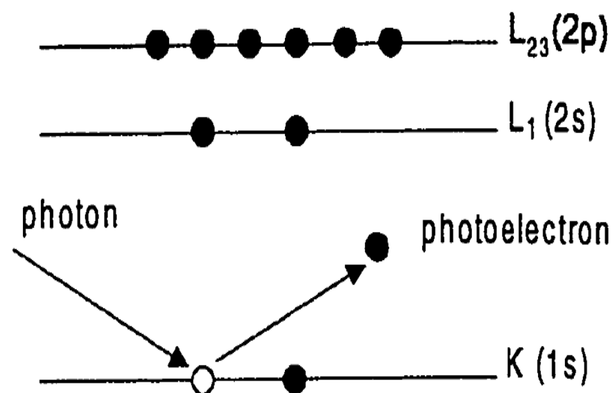

Figure 5.4: *XPS emission for a model atom [52].*

Governing this process is the well-known but modified Einstein equation for the photoelectric effect expressed as

$$E_{KE} = h\nu - E_B - W \quad (5.4)$$

where E_{KE}, $h\nu$, E_B, and W are the energies of the ejected electron, the incident photon, the involved bound electron state, and the work function difference between sample and detector. Since values of the binding energy are element specific, atomic identification is possible through measurement of photoelectron energies. The following table summarizes capabilities and limitations for particular analytical applications.

Table 5.1: *Summary of XPS capabilities and limitations.*

Elemental sensitivity	**Detection limit (at.%)**	**Lateral resolution (μm)**	**Effective probe depth (Å)**
Li-U	~0.1-1	~100	15

One very useful capability for thin-film analysis is depth profiling. It is accomplished with incorporated ion guns that enable the sample surface to be continuously sputtered away while the ejected electrons are being simultaneously detected. Multi-element composition depth profiles can then be determined over total film thicknesses of several thousand angstroms by sequentially sampling and analyzing film layers. While depth resolution is extremely high, the frequently unknown sputter rates make precise depth determinations problematical.

Quantitative analysis of an element in a multi-component matrix is a complicated matter. External standards are important in quantifying elemental analysis since excellent computer programs are available for analysis and compositions are typically computed to approximately 1 at.%. A formula which has been widely used to determine the atomic concentration of a given species A in a multi-element matrix is

$$C_A = \frac{N_A / S_A}{\sum_{i=A,B...} N_i / S_i} \tag{5.5}$$

The quantity N_i represents the counts of the XPS peak. Relative XPS sensitivities, S_i, also enter Eq. 5.5.

Furthermore, XPS is capable of readily providing information on the nature of chemical bonding and valence states, due to its linewidths are considerably narrower than the other surface analytical techniques (EDX, AES, etc.). Effects due to chemical bonding originate at the valence electrons and ripple beyond them to alter the energies of the core levels in inverse proportion to their proximity to the nucleus. As a result, energy shifts of a few eV occur and are resolvable.

5.5 Time-of-flight secondary ion mass spectroscopy

Time-of-fight secondary ion mass spectroscopy is a surface sensitive technique that analyzes the chemical composition of solid surface layers. A critical need to measure thermally diffused and ion-implanted depth profiles of dopants in semiconductor devices spurred the development of SIMS. In typical devices, peak dopant levels are about $10^{20}/cm^3$ while background levels are $\sim 10^{15}/cm^3$. These correspond to atomic concentrations in Si of 0.2% to 2×10^{-6}%, respectively. None of the analytical techniques considered so far has the capability of detecting such low concentration levels. The price paid for such high sensitivity is a complex spectrum of peaks corresponding to the masses of detected ions and ion fragments.

ToF-SIMS is the destructive removal of material form the sample by sputtering of the sample and the analysis of that material by a mass spectrometer. Fig. 5.5 shows the sputtering phenomenon. As energetic primary ion incident on sample, the energy is transferred to the atoms in the sample by collision. After a cascade of collisions occurs between the atoms, some collisions return to surface and result in emission of particles. These secondary particles, electrons, neutral species, atoms, molecules, and cluster ions, are collected and separated by their mass-to-charge ratio using a sensitive spectrometer. Argon (Ar^+), oxygen (O_2^+), cesium (Cs^+), and gallium (Ga^+) are the most common primary ions.

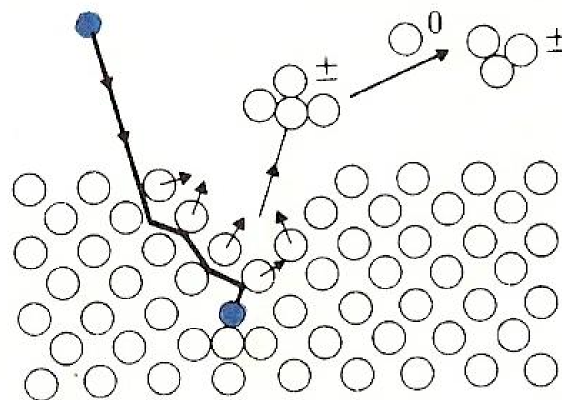

Figure 5.5: *ToF-SIMS, Primary ion strikes the sample surface and yields secondary particles (atoms, ions, and melecules).*

The uniqueness of ToF-SIMS above SIMS itself rests upon the mass analyzer and the level of the dose of primary ions for sputtering. The primary ions are pulsed with doses less than 10^{13} ions/cm^2 and fluxes less than 50 nA which implies that there is only a small probability that more than one primary ion will strike the same area [53]. The pulsed secondary (sputtered) ions are accelerated at a potential V (3 to 8 keV) such that all ions possess the same kinetic energy. For ions of charge z, mass m,

traveling along a tube of length L_T, the ions equation of motion for the ions yields the time of flight as

$$t = L_T \left(\frac{m}{2zV} \right)^{1/2} \quad (5.6)$$

Thus, the time at which the ions strike the detector depends on their mass, and all the masses are extracted in coincidence. This detection system leads to mass resolutions greater than $m/\Delta m > 4000$.

The sputter yield is the average number of sputtered atoms per incident ion. The sputter yield depends on the energy deposition near the surface, the number of recoils created, surface barrier height or surface binding energy, the masses of the incident ion and the sputtering atom, as well as the incident and ejection angles. Modeling combined with experiments has been exploited to quantify the sputter yield for pure elements and various compounds [54]. However, for impurity and dopant atoms inside a material, the sputter yield depends strongly on the local environment of the atom inside the material as well as on the ion-sample interactions. A common rule of thumb is that the standard deviation of the sputter yield is of that same order of magnitude as the average sputter yield. Also the sputter yield varies by orders of magnitude from element to element inside the sample (matrix). This necessitates the use of standards, composed of the specific elements and matrices in question, for quantitative determinations of composition.

Since it is the secondary-ion emission current which is detected in SIMS, high sensitivity analysis requires methods for enhancing sputtered ion yields. Experimentally, it has been found that different ion beams interact with the specimen

surface in profoundly different ways. For example, the positive metal ion yield of an oxidized surface is typically enhanced tenfold and frequently more, relative to a clean surface. This accounts for the common practice of using O_2^- beams to flood the surface when analyzing positive ions. Similarly, the negative ion signals can be enhanced by using Cs^+ primary ion beams. One of the theories which attempt to explain the opposing effects of O_2^- and Cs^+ beams involves charge transfer by electron tunneling between the sample and ions leaving the sample surface. Negative ion (O_2^-) bombardment repels charge from the surface, in effect lowering its Fermi energy and raising its effective work function. Tunneling is now favored from the surface atom (soon to be an ejected positive ion) into the now-empty electron stats of the sample. Similarly, positive ion (Cs^+) bombardment lowers the target work function. Now electrons tunnel form the sample into empty levels of surface atoms, enhancing the creation of negative ions. Since these charge transfer processes depend exponentially on the effective work function, very large changes in ion yields with small shifts in the effective work function are possible.

5.6 Photoluminescence spectroscopy

One of the most important characteristics of Er-doped a-C:H is its ability to exhibit room-temperature photoluminescence (PL). Photoluminescence spectroscopy, which is employed to detect the PL signal, is an experimental technique that uses photo-excitation and de-excitation of carriers to determine the optical, electrical, and structure properties of materials. The Er luminescence mechanism has been discussed in section 3.2. The apparatus for measuring PL consists of an excitation source, a monochromator, and an optical detection system. A block diagram of this system is shown in Fig. 5.6. The three main components are described in detail below:

a) ***Excitation source***

The optical excitation source is an Innova 90 CW Ar^+ ion laser which is operated at 512 nm.

b) ***Monochromator***

The Perkin-Elmer model E1 grating monochromator is used to measure the luminescence signal. With visible and near-infrared grating, the spectral range of the monochromator extends from 400 to 1700 nm.

c) ***Optical detection system***

The transformation and amplification of the optical signal to an electrical signal are accomplished by an optical detection system which includes a photodetector to convert the photon energy to an electrical signal, and a lock-in-amplifier and an optical chopper (Newport SR 540) to filter and

amplify the photo-generated electrical signal. The Er luminescence is in the range of 1400 -1650 nm; a TE-cooled InGaAs photodetector (EOS IGA-020-TE2) with a pre-amplifier and a spectral response in the range of 850 – 1650 nm will be used to detect the optical signal. A Labview code implemented software was used to interpret the acquired data.

During the measurement, the laser beam with ~600 mW is focused down to ~1 mm at the surface of films. The size of the input and output slit of the monochromator is 70 μm which provides extremely high spectral resolution. Further increasing the slots can boot up the PL signal, however no improvement on the signal-to-noise ratio.

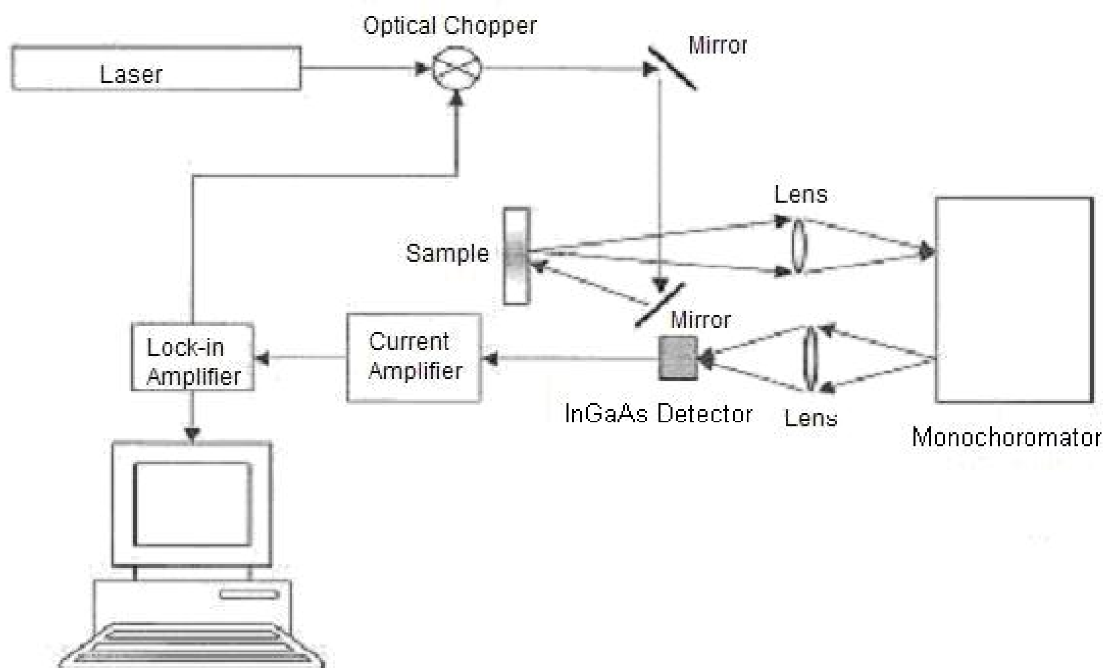

***Figure 5.6**: Photoluminescence Spectroscopy apparatus.*

Chapter 6

Erbium complex doped amorphous carbon: Results and Discussion

6.1 a-C:H doped with Erbium 2,4-pentanedionate

Erbium 2,4-pentanedionate ($Er(acac)_3$) obtained from Alfa Aesar (item #13214) was first chosen as an Er dopant. In order to investigate its suitability, ten Er doped a-C:H films were deposited using the gas mixture (methane + $Er(acac)_3$) (Table 4.2). Table 6.1 lists the amount of $Er(acac)_3$ evaporated during each of the depositions. To study the effects of the deposition parameters on the Er evaporation, the films can be divided into four subgroups for the analysis.

The evaporation results suggest that an increase in the evaporator temperature results in a relatively small increase in the Er evaporation rate (subgroup 1), whereas the chamber pressure, the flow rate and the anode current do not play an important role in this case (subgroups 2-4). The color of the powder ($Er(acac)_3$) changed from off-white to yellow when the temperature was increased to around 115 ˚C, and afterwards, the powder became sticky and formed mm-size clusters at around 125 ˚C and the color turned orange, and for >145 ˚C, the clusters turned black. Fig. 6.1 shows the ramping of the evaporator temperature and the powder consumption for

sample B1. The powder sublimation only occurred primarily in the first 10 minutes of the deposition time, and around 80% of the powder was left in the boat. This is consistent with the SIMS analysis that reveals the presence of less than 10^{-3} at.% of the Er atoms or compounds during the initial stage of film growth, approximately 10 nm (Fig. 6.2).

Table 6.1: *Amount of Er(acac)3 evaporated during each of the depositions.*

Sample	B1	B2	B3	B4	B5	B6	B7	B8	B9	B10
Amount of Er(acac)$_3$ evaporated (mg)± 1mg	5	5	7	8	3	3	5	5	5	5

Subgroup 1: B1-B6
Subgroup 2: B1, B7 and B8
Subgroup 3: B1 and B9
Subgroup 4: B1 and B10

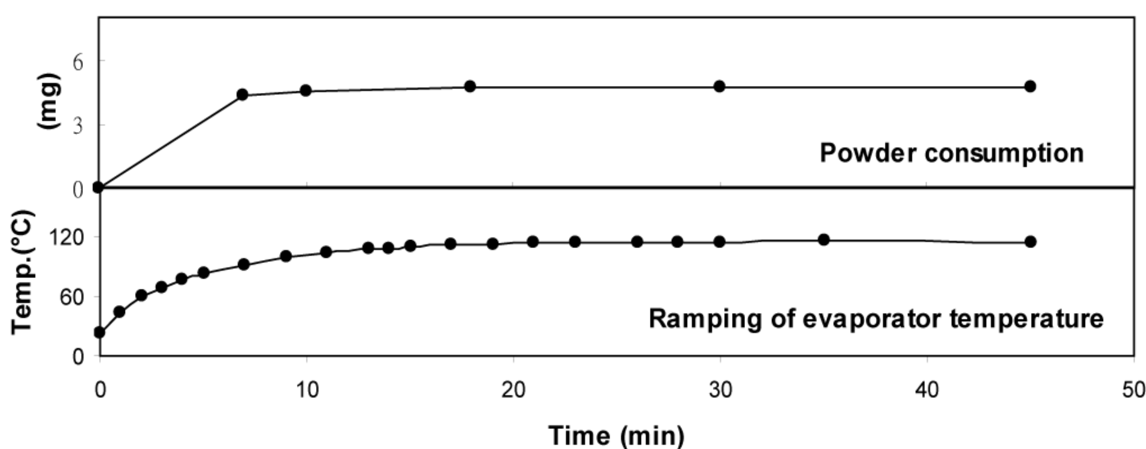

Figure 6.1: *Ramping of evaporator temperature and Er(acac)$_3$ powder consumption with deposition time for sample B1.*

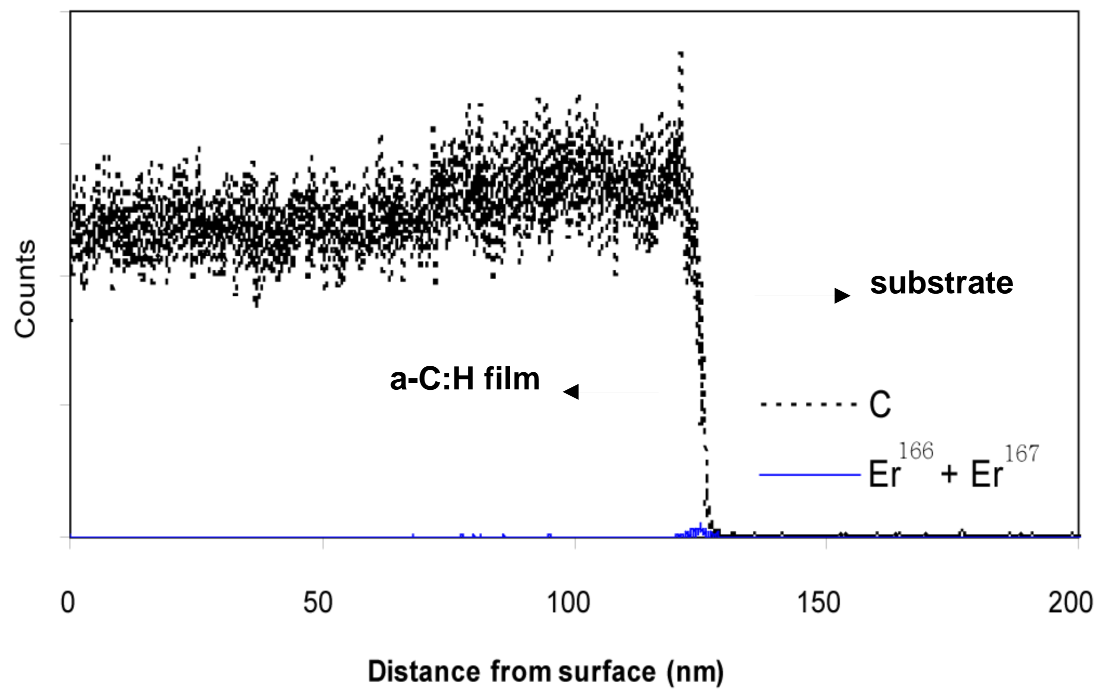

Figure 6.2: *SIMS result for sample B1.*

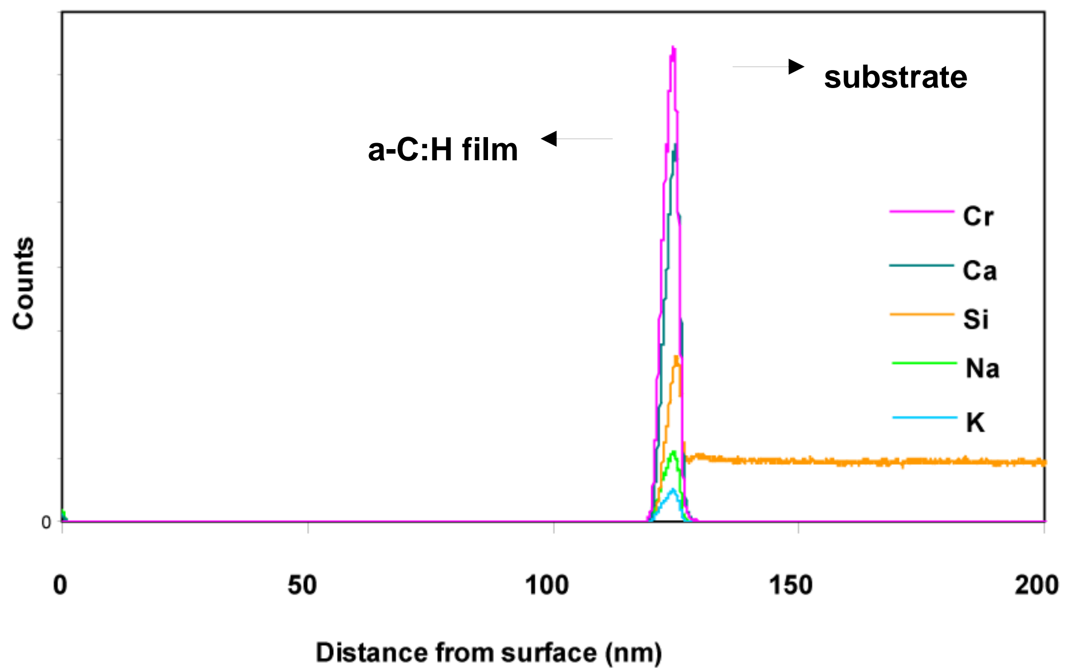

Figure 6.3: *SIMS result indicates the contaminations.*

The carbon content stays constant as a function of depth, and then falls off upon reaching the substrate. The steep slope at around 125 nm from the surface indicates the film-substrate interface where the detectable amount of Er was found.

There was no Er luminescence was detected from any of the samples. The thermal annealing of the samples in atmosphere resulted in peeling of the films from the substrates because of C (film) - O_2 (air) chemical reactions. On the other hand, interesting results were found regarding contamination sources. As seen in Fig. 6.3, significant presence of Cr, Ca, Na, and K were observed in the film during the early stages of its growth: i.e. at the film-substrate interface, caused by imperfect cleaning for electrodes, resulting in incorporation of unwanted spices sputtered from the electrodes during the Ar discharge pre-cleaning before film growth. Note the Si content, approaching from the substrate, starts off flat and then picks up upon reaching the interface. This rapid rising indicates that there is a structure change at the interface, affecting the work function, the density, the electronegativity and the ionization energy in the local network, and hence the sputter yield of a given element. This contamination problem at the interface can be eliminated by installing a shutter assembly which covers the entire substrate holder and protects samples from the discharge during the Ar discharge pre-cleaning.

Based on the above experiment results, $Er(acac)_3$ is not suitable for the doping method used in this project, due to its poor volatility and thermal stability. It could encounter hydrolysis and polymerization when heated, which results in progressively diminishing the vapor pressure [55]. Irina et al. proposed that a stable volatility could be achieved in chemical systems which provided coordinational saturation of lanthanide [56]. In his paper, anionic complexes were used as volatile species of rare

earth element (REE) acetylacetonates (acac). The coordination saturation of the REE central ion in this case occurs through the addition of the fourth acetylacetonate chelate cycle to form $LiEr(acac)_4$ compound. The sublimation degree of $LiEr(acac)_4$ was large. There appears to be a process of $LiEr(acac)_4$ dissociation with formation of Li(acac) and $Er(acac)_3$, hence their sublimation accompanied by partial decomposition when heated in vacuum take place.

6.2 Luminescence of $Er(TMHD)_3$ in KBr pellet and in methanol

In spite of the unsuccessful sublimation of $Er(acac)_3$, $Er(TMHD)_3$ was chosen as an alternative Er source. The investigation began with the experiments focusing on its volatility and luminescence properties. First, the sublimation of $Er(TMHD)_3$ could be achieved when heated above 120 ˚C in vacuum, and the condensation on the chamber walls and the electrodes was observed. Secondly, the photoluminescence spectra of 0.5, 1, 2, 5, and 10 mol% of $Er(TMHD)_3$ diluted in KBr and that of 2 mol% in methanol were measured and compared and is shown in Fig. 6.4. The peak at 1545 nm, is the transition between the $^4I_{13/2}$ level and the $^4I_{15/2}$ state. All the peak position and the fine structure are the same. The emission intensity increases with the Er concentration, and starts to saturate for that with the Er concentrations above 5 mol%. Furthermore, the low signal intensity from 2 mol% of Er in methanol indicates an optical quenching effect which will be discussed in the following sections.

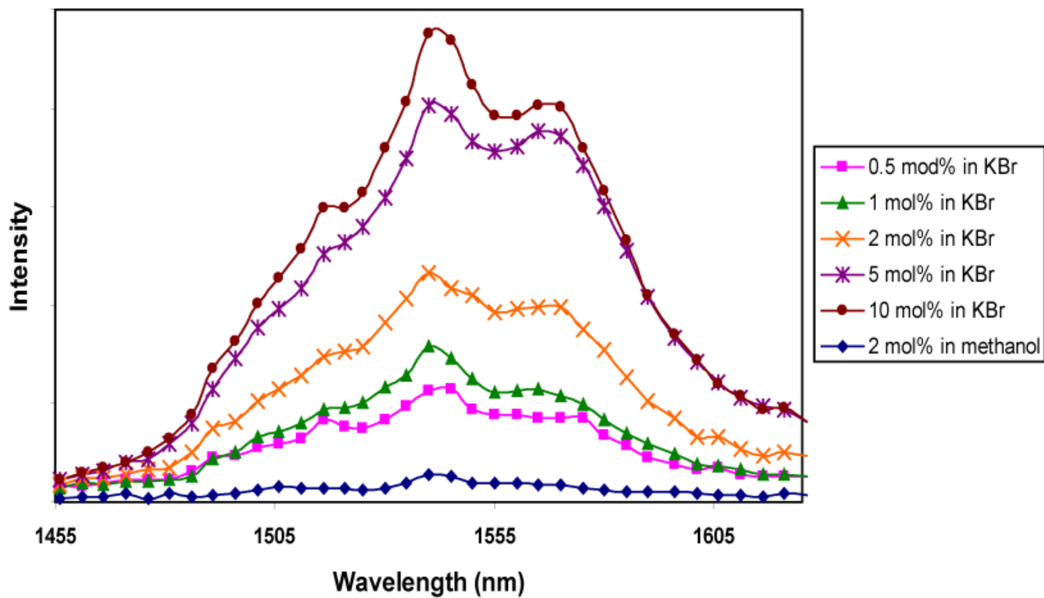

Figure 6.4: *Comparison with emission spectra of Er(TMHD)$_3$ in KBr and methanol.*

6.3 a-C:H doped with Er(TMHD)$_3$

In order to established a set of suitable deposition conditions to achieve high concentration Er doping and to produce a homogenous Er depth profile in the Er doped a-C:H films, six Er doped a-C:H films were deposited using the gas mixture (methane + Er(TMHD)$_3$) (Table 4.3). The Er content of the deposited films was controlled by the evaporator temperature and the amount of the powder loaded. In this section, a complete deposition conditions tuning process is present, and the results are discussed.

Sample E1

The deposition conditions used to prepare sample E1 are listed in Table 4.1 and 4.3, and the deposition lasted for 80 minutes. To test the thermal stability and to establish a monotonic/continues evaporation of the powder within a temperature range (i.e. 110-130 ˚C); the evaporator temperature was slowly increasing the evaporator temperature during the deposition. At the end of deposition, the boat loaded with power was depleted. Fig. 6.5 shows the ramping of the evaporator temperature while Fig. 6.6 shows the SIMS depth profile of the Er concentration. As seen in the Er depth profile, the detectable Er content start to reveal at ~50 nm away from the film-substrate interface and then smoothly increase until the Er reservoir is depleted. This is consistent with the evaporator temperature, which reached to 125 ˚C at 15 minutes after deposition started. The powder was thermal stable and did not dissociate which could diminish the vapor pressure, at the same time it was in a controllable evaporation condition during the deposition. PL measurement was carried out on this sample, no emission around 1.54 μm was observed, and therefore the amount of powder loaded was increased and constant evaporator temperature was kept during the next deposition.

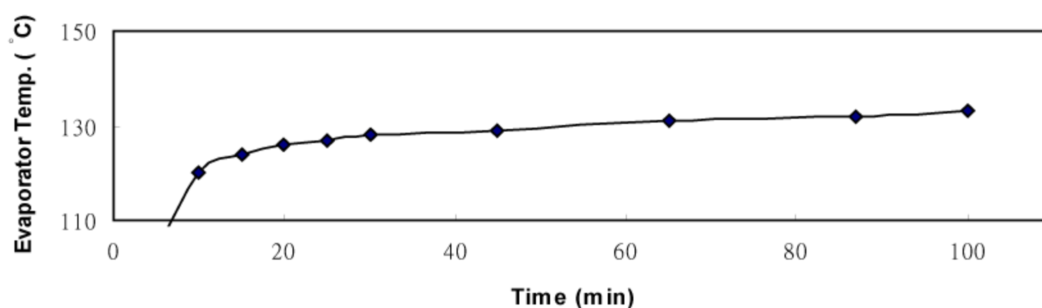

Figure 6.5: *Evaporator temperature ramping for sample E1.*

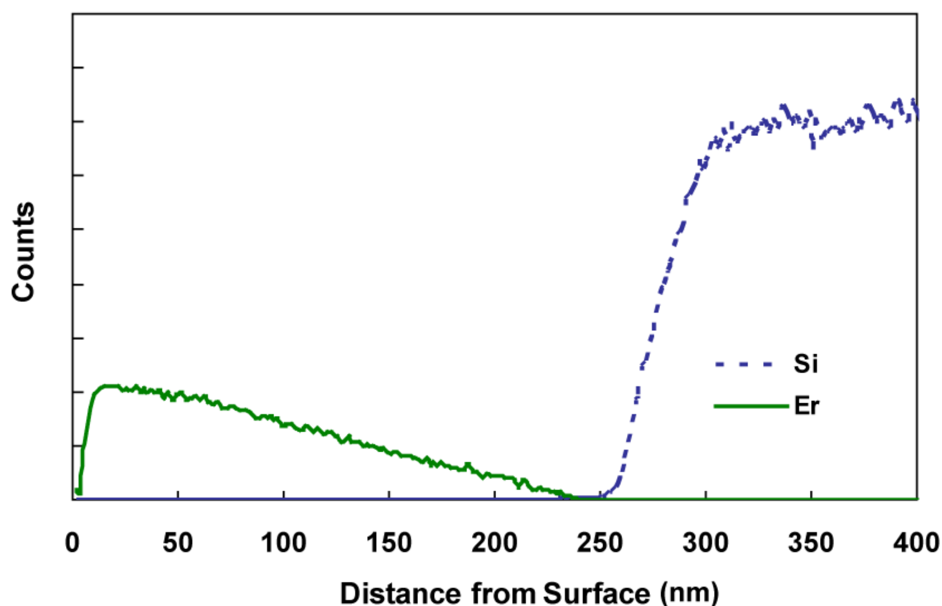

Figure 6.6: *Depth profile of sample E1 determined by SIMS.*

Sample E2

For this sample, XPS analysis was carried out and Fig. 6.7 shows the Er and O concentrations as a function of the distance from the film surface. The film was 310 nm. In spite of the low Er concentration (0.11-0.18 at.%), the Er distribution is relatively homogeneous compared to last sample. The Er and O distribution are comparable: they are almost identical in the region from 50nm to 230nm suggesting that the source of O is mainly originated from the metal-organic ligands. The falling of the Er concentration near the surface is associated with the depletion of the Er reservoir; on the other hand the increase of the O concentration near the surface could be caused by the surface contaminations. Apparently, there are some C and O contaminations in the Si substrate. However, this sample did not exhibit the Er luminescence suggesting more Er content or an Er thermal activation is required.

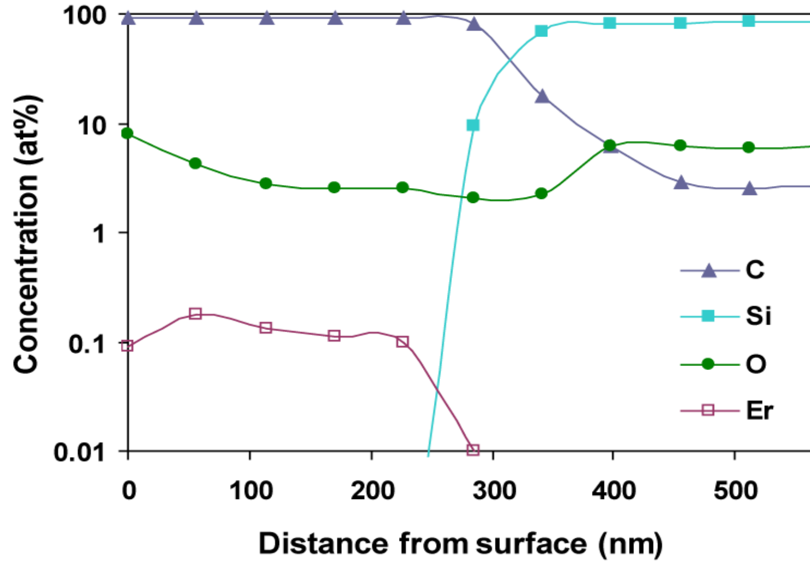

Figure 6.7: *C, Si, O, Er and O concentrations as function of the distance from the film surface as determined by XPS (sample E2).*

Sample 3

Additional 28 mg of the powder was loaded and the evaporator temperature was increased to 137 ˚C from 134 ˚C for this film deposition. This sample was subjected to a post-thermal annealing treatment at 100, 200, 300, 400 ˚C in an H_2 environment for 15 minutes. The H_2 flow was 40 sccm while the chamber pressure was maintained at 1 Torr. It has been shown that a-C:H films annealed in H_2 have greater optical properties than that annealed in vacuum [57]. The substrate holder takes 8-15 minutes to ramp up to a desired temperature. The annealing time is defined as time when desired temperature is reached. PL measurements were performed on the samples annealed at different temperature. The PL spectra for the annealed and non-annealed samples are shown in Fig. 6.8. For all of the samples, no Er emission band was observed. The PL intensity increases as the annealing temperature (T_A) increases for

$T_A \geq 300$ ˚C , whereas, for $T_A < 300$ ˚C, the intensities are almost the same. This increase in PL intensity in the near IR region can be explained by the fact that a-C:H films exhibits a strong visible PL at room temperature and a tail extended into near IR region, and this band experiences a red shift as annealing temperature increases above 250 ˚C [58].

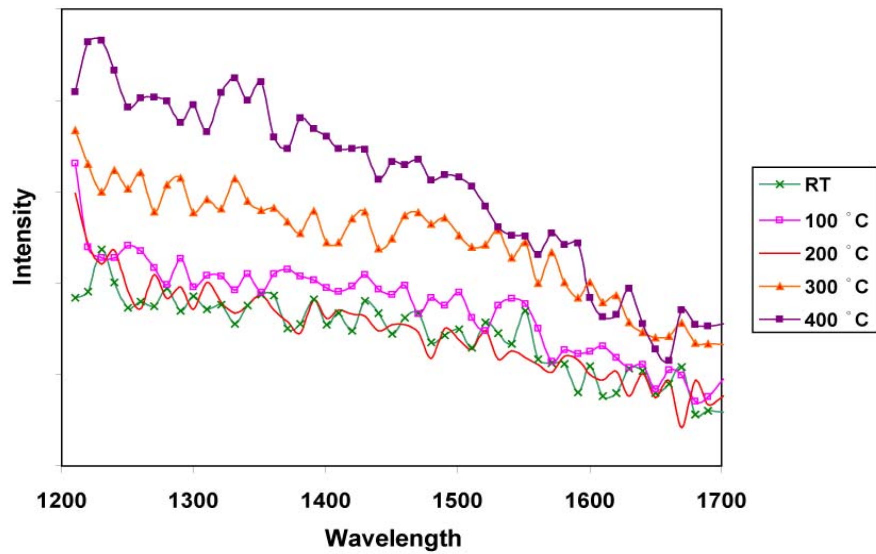

Figure 6.8*: PL spectra for the annealed and non-annealed samples of E3.*

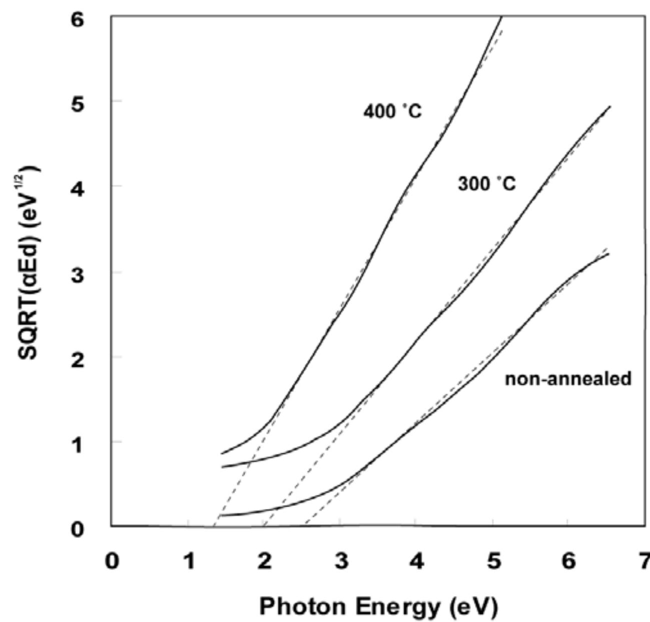

Figure 6.9: *Tauc plot of sample E3 annealed at different temperature in H_2 to determine the optical bandgaps.*

To give further support to this interpretation, such red shift is consistent with the optical bandgap (E_g) results which are determined by the method discussed in section 5.3 and shown in Fig. 6.9. As seen in Fig. 6.9, the value of E_g decreases from 2.5 to 2 and 1.3 eV as T_A increases to 300 and 400 ˚C, respectively. As T_A increases above 300 ˚C, the size of the sp^2 graphitic clusters increases and becomes dominant in the sp^3 a-C:H network, causing a decrease in E_g (as a bandgap of a pure graphite is zero). This enhancement in sp^2 graphitic clusters can be explained by an evolution of hydrogen from the film [59]. Since the PL in a-C:H arises within the cluster, the PL peak energy should reflect the most favorable cluster size in the a-C:H film; smaller bandgaps shift the PL peak energy towards lower energy. Therefore, as the bandgap decreases with increasing cluster size, the PL peak energy decreases.

On the other hand, the bandgaps stay relatively constant for $T_A \leq 200$ ˚C in a range from 2.6 to 2.5 eV, hence the effect on the PL intensity is not significant. This is also consistent with the results reported by N.M.J. Conway et al. [60]; at low annealing temperatures up to ~ 300 ˚C, there was no significant effusion of hydrogen from the films or major changes in structure were observed.

Sample 4 - 6

The amount of the powder loaded was increase to 175 mg for sample E4, 504 mg for E5 and 787 mg for E6. The evaporator was kept at 145 ˚C for sample E4, and at 160 ˚C for sample E5 and E6. The films appear to be good surface quality, but non-uniformity of films occurred as the evaporator temperature increases above 145 ˚C as seen in Fig. 6.10. There is a thickness gradient across the film, and it is worth while to perform measurements at different spots. The measurement results of E5a were extracted at a spot 10 cm in front of the Er reservoir, and 11 cm for that of E5b. The characterization results have been summarized in Table 6.2.

Figure 6.10: *A picture of sample E4.*

Table 6.2: *Summary of characterization results of sample E2 – E6.*

Sample	*Avg. Er conc. (at.%)*	*Avg. O conc. (at.%)*	*Amount of Er(TMHD)$_3$ loaded (mg)*	*Evap. Temp. (℃)*	*Growth rate (nm/min)*
E2	0.15	4	41	134	2.7
E3	-	-	69	137	2.9

E4	0.37	5.5	175	145	3
E5a	1.88	13	504	160	6
E5b	1.5	12.3	504	160	3.5
E6	0.3	5.2	787	160	2.8

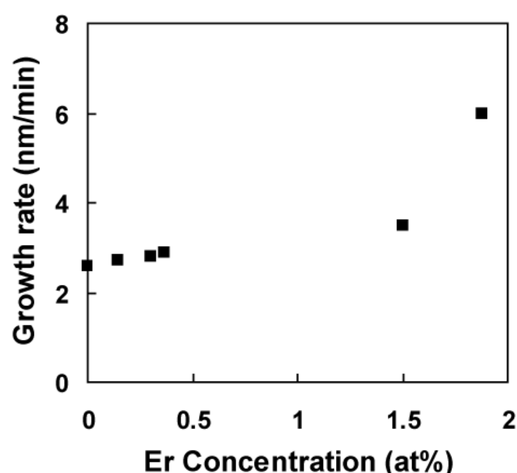

Figure 6.11*: Growth rate of the films as a function of Er concentration.*

A graph of growth rate as a function of Er concentration in the film is shown in Fig 6.11. The growth rate starts at 2.6 nm/min for an undpoed film and increases with increasing Er concentration to 6 nm/min at an Er concentration of 1.88 at.%. The film formation is mainly orginated from the metal-organic ligands at high doping levels.

The doping profiles of Er and O of sample E4- 6 were investigated with the aid of XPS analysis. The XPS depth profiles of major elements in the films are shown in Fig. 6.11 – 6.14. The uniformity of the Er concentration during film growth was independent of the film thickness, the amount of Er powder loaded and the evaporator temperature, with the exception of E6 which will be discussed. The sublimed Er

source system is delivering a relatively constant amount of Er to the chamber during the growth period. Oxygen concentration profiles follow the same trend as the Er profiles with the exception of an increase at the surface due to the surface contaminations. The O/Er ratios in different samples were compared. A graph of raito for O/Er atoms as a function of Er concentration is shown in Fig 6.15. The ratio of O/Er atoms starts at 26.6 for an Er concentration of 0.15 at.% and decreases with increasing Er concentration until a ratio of 6.9 is reached at an Er concentration of 1.88 at.%. The ratio for O/Er atoms in the $Er(TMHD)_3$ compound is six, indicating that an additional source of oxygen in the process which is significant at low doping levels, or that the ligands of the metal-organic are breaking up and are being incorporated into the film at low doping levels. Only at high doping levels does the correct ratio of O/Er appear in the film. At low doping levels, the result is disappointing from the perspective of incorporating intact, optically active ErO_6 fragments. Energetic ions or electrons in the plasma collide with the metal-organic molecule and cause it to dissociate, both in the gas phase or adsorbed on the film surface. Hydrogen radicals created by the dissociation of methane in the discharge are highly reactive. There radicals could react with the carbon in the metal-organic ligands and also play a role in the dissociation of the metal-organic ligands [61].

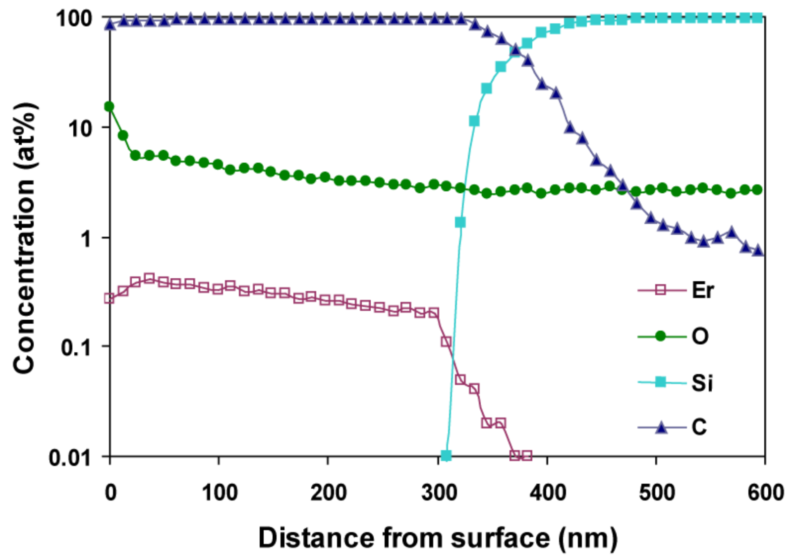

Figure 6.12: *C, Si, O, Er and O concentrations as function of the distance from the film surface as determined by XPS (sample E4).*

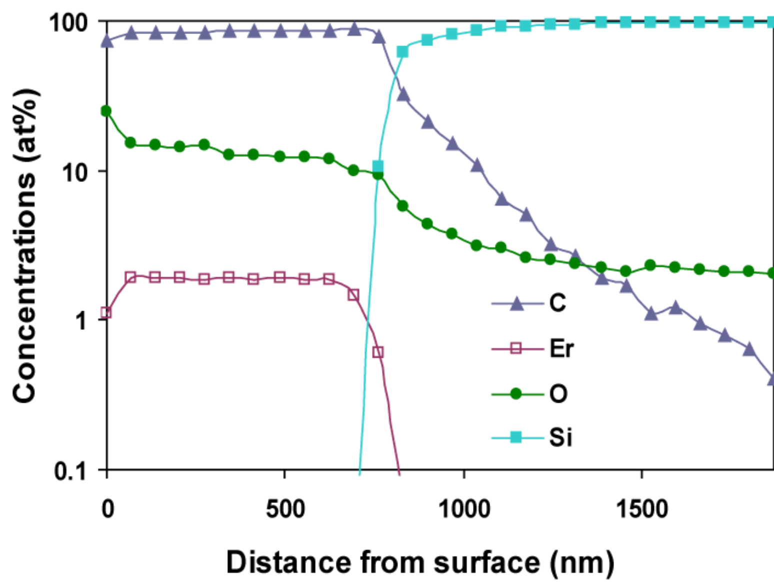

Figure 6.13: *C, Si, O, Er and O concentrations as function of the distance from the film surface as determined by XPS (sample E5a).*

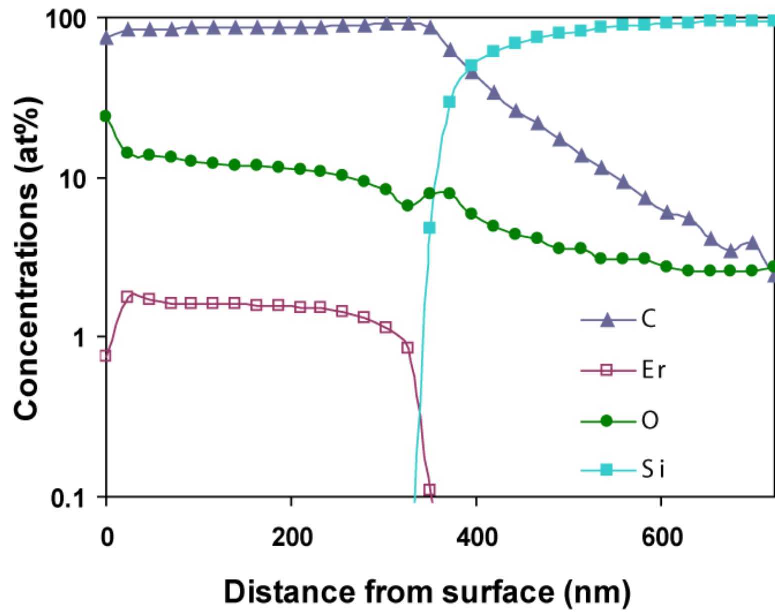

Figure 6.14: *C, Si, O, Er and O concentrations as function of the distance from the film surface as determined by XPS (sample E5b).*

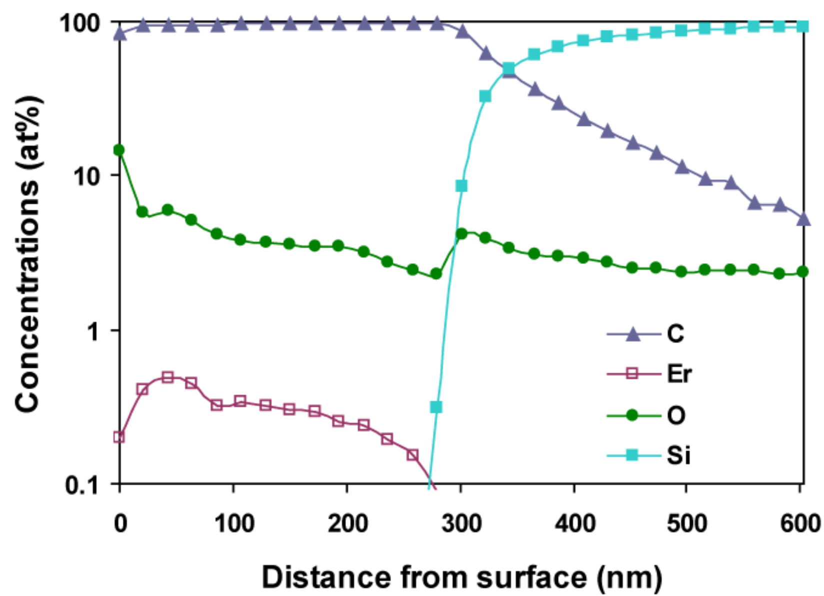

Figure 6.15: *C, Si, O, Er and O concentrations as function of the distance from the film surface as determined by XPS (sample E6).*

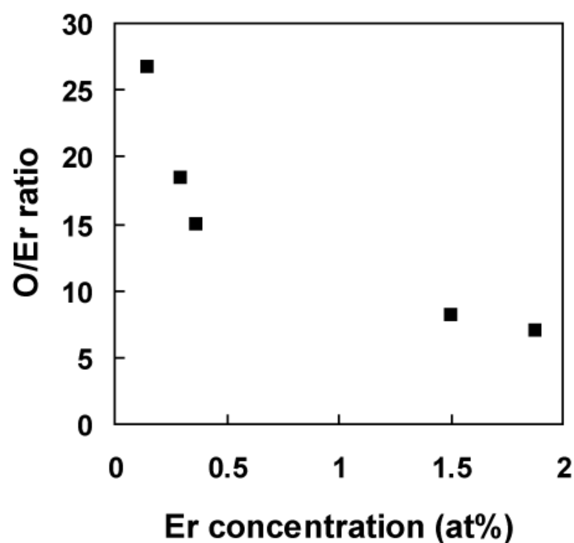

Figure 6.16: *O/Er ratio in the films as a function of Er concentration.*

Sample E4 and E5 were also subjected to a thermal annealing treatment. However no detectable Er emission was observed for both samples and the PL spectra resemble the same conclusions were drown from the thermal analysis of sample E4.

The unexpected inhomogeneous and low doing Er concentration of sample E6 (Fig. 6.15) is due to the fact that the most part of sublimated metal-organic were condensed inside the wall of the guiding tube, forming an obstacle in the pathway towards the substrate. Therefore, the guiding tube was discarded, and hence higher Er concentration can be achieved.

Sample E7

A picture of sample E7 is shown in Fig. 6.17. The non-uniformity of the film was created intentionally to find an Er concentration at which Er luminescence is detectable. As seen in Fig. 6.17, the thickness and the Er concentrations increase from left to right. Any spot to the right of the arrow exhibits exhibit room-temperature Er luminescence. The block arrow points at a spot with Er concentration of 2.04 at.% and the signal to noise ratio at this spot is 1.4 (Fig. 6.18). In other words, an Er concentration of 2.04 at.% (M_H) is the minimum doping requirement to see Er emission in Er-doped a-C:H films made in the present work. In addition, The metal-organic dominated film growth in the film region to the right of the arrow resulted in a poor surface quality. Although, the film eventually revealed to satisfy the emission requirement, however the poor surface quality still makes a-C:H a unsuitable host material for Er.

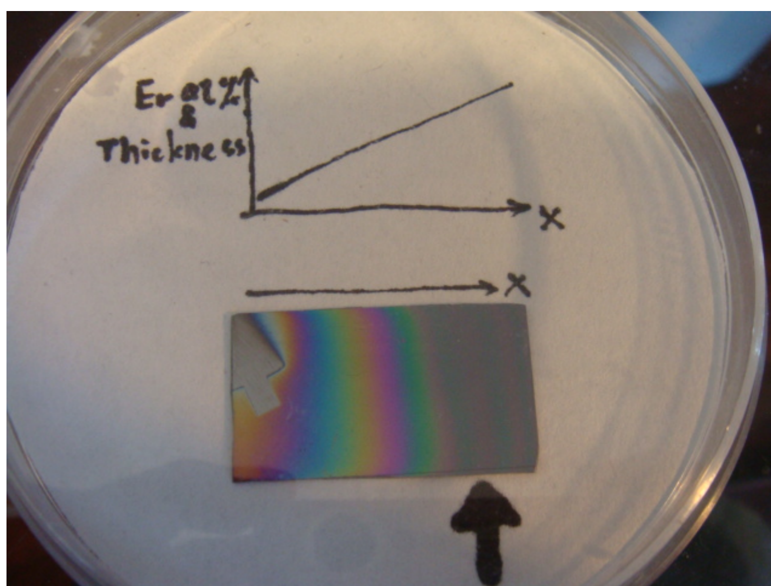

Figure 6.17: *A picture of sample E7 and an arrow indicates a spot, the film to the right of this spot exhibits Er luminescence.*

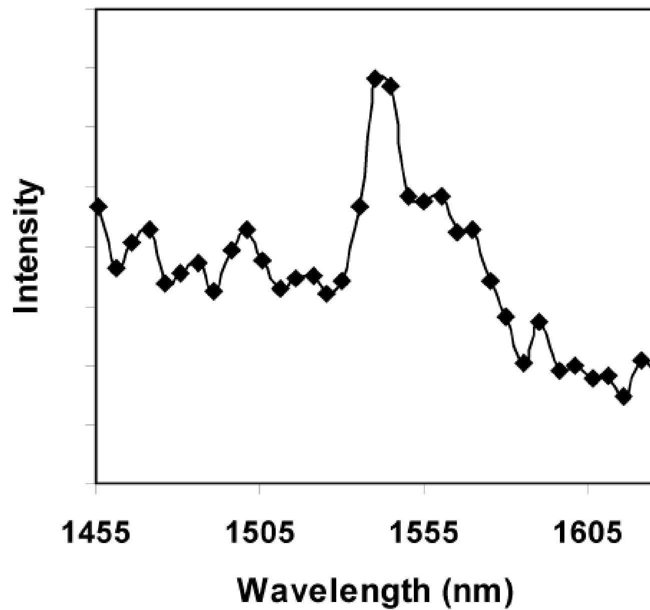

Figure 6.18: *PL spectrum for the films with Er concentration of 2.05 at.%.*

6.4 Luminescence quenching effect

Erbium metal-organic complex has been very attracting for the development of low-cost light sources and infrared amplifiers to integrate in planar photonics circuits for optical communications, because of its properties discussed in section 3.3. However, its ligands and organic solvent usually contain C-H and O-H bonds, and near-infrared emission quenching is mainly attributed to the coupling of the excited state of the Er^{3+} ion with high frequency vibrations of CH and OH groups [62]. The energy gap of the radiative transition in Er^{3+} ion (~ 6500 cm^{-1} between the ground state $^4I_{15/2}$ and the first excited state $^4I_{13/2}$) approximately matches the second harmonics of C-H and O-H bond vibrations (5900 and 6900 cm^{-1}, respectively) of

host material. Substitution of hydrogen with heavier deuterium atom which lowers the vibration frequency could be a possible strategy to reduce the induced emission quenching. The important of C-D vibrations on the quenching can be seen from Fig. 6.19, where we schematically show the relative energies of the quenching transition for Er^{3+} ion along with the energy of the C-H and C-D vibrations and their harmonics. By doing this, the harmonic number was modified by deuteration from v= 2 (C-H and O-H) tov= 3 (C-D and O-D). For erbium ion to be quenched, it appears that the role of C-D is less important as it is the third harmonic.

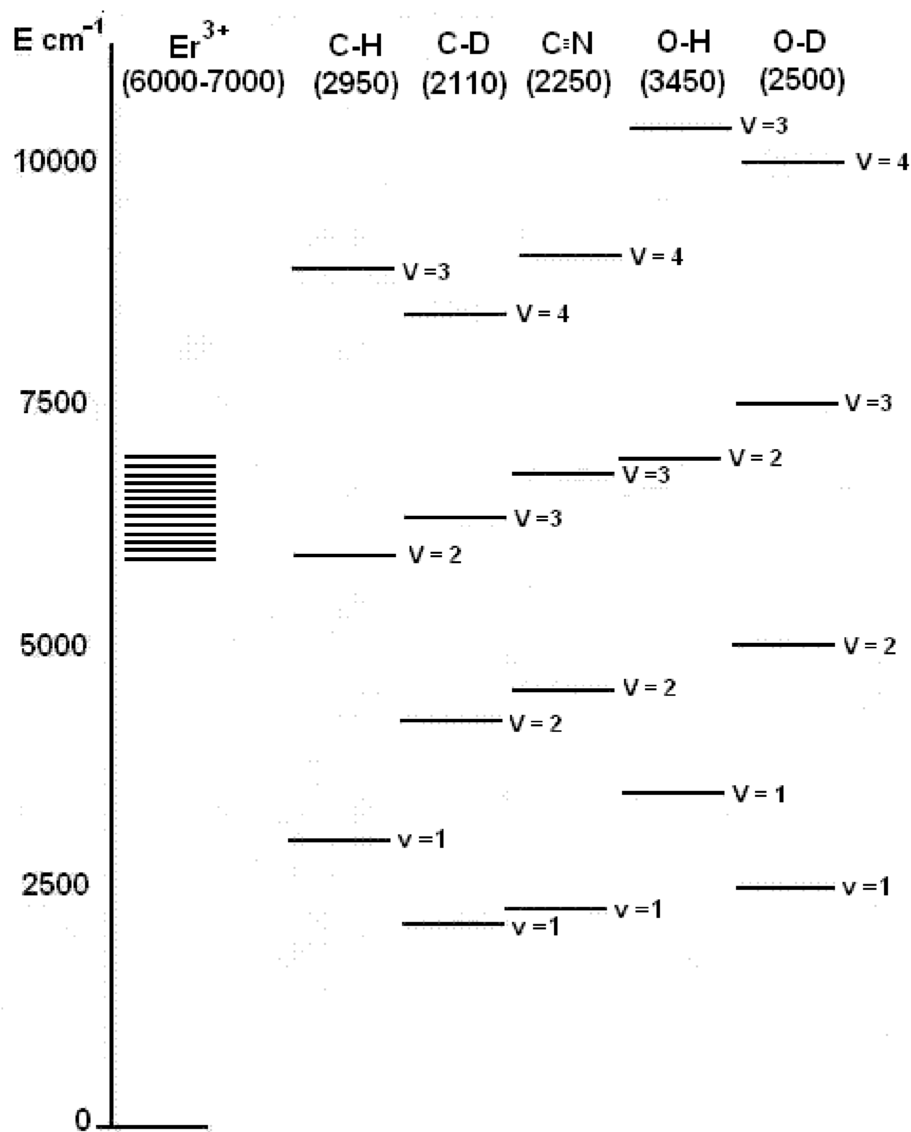

Figure 6.19: *Schematic presentation of the vibrational energy levels in organic media and matching the electronics energy gap of* Er^{3+} *ion.*

6.5 Effect of deuterated material system on Er^{3+} emission

To investigate the effect of removing C-H and O-H vibrations in the host material on the Er luminescence properties, the PL spectra of 1.1 mol% of $Er(TMHD)_3$ in methanol were compared with that in deuterated methanol as shown in Fig. 20. The deuteration of the methanol (host material) provides one order of magnitude enhancement in the Er luminescence. The effect of deuteration significantly decreases the probability of non-radiative transitions of Er ions; the Er luminescence properties are strongly depends on the immediate local environment. This promising result suggest that the same strategy could be applied to the Er doped a-C:H material system.

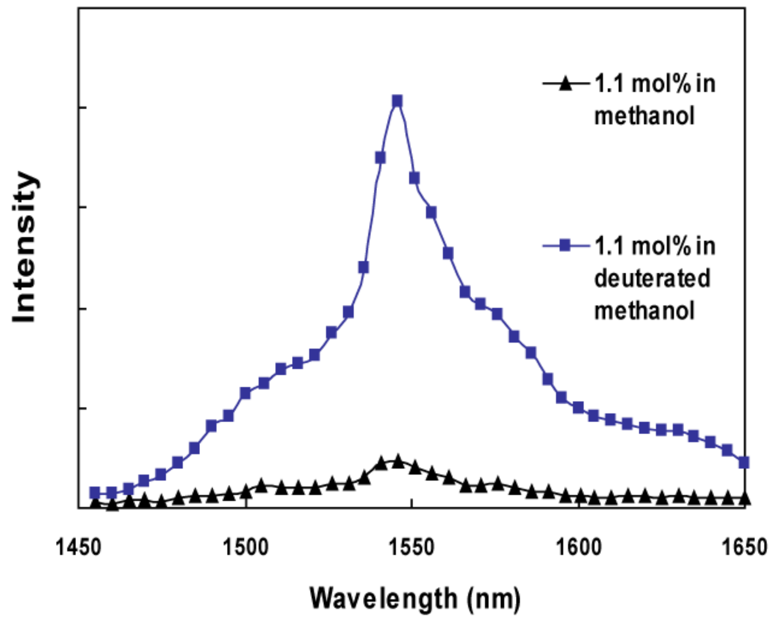

Figure 6.20: *Comparison with PL spectra for 1.1mol% of Er(TMHD)$_3$ in methanol and that in deuterated methanol.*

In spite of the non-uniformity of film, one film deposition can be used to study the correlation between the Er emission and the Er concentration. This last sample, called Er-doped a-C:D, was prepared using the gas mixture (Er(TMHD)$_3$ + CD_4). The characterization measurements were performed on four different spots (Fig. 6.21). Table 6.3 lists the atomic concentration results associated with the spots.

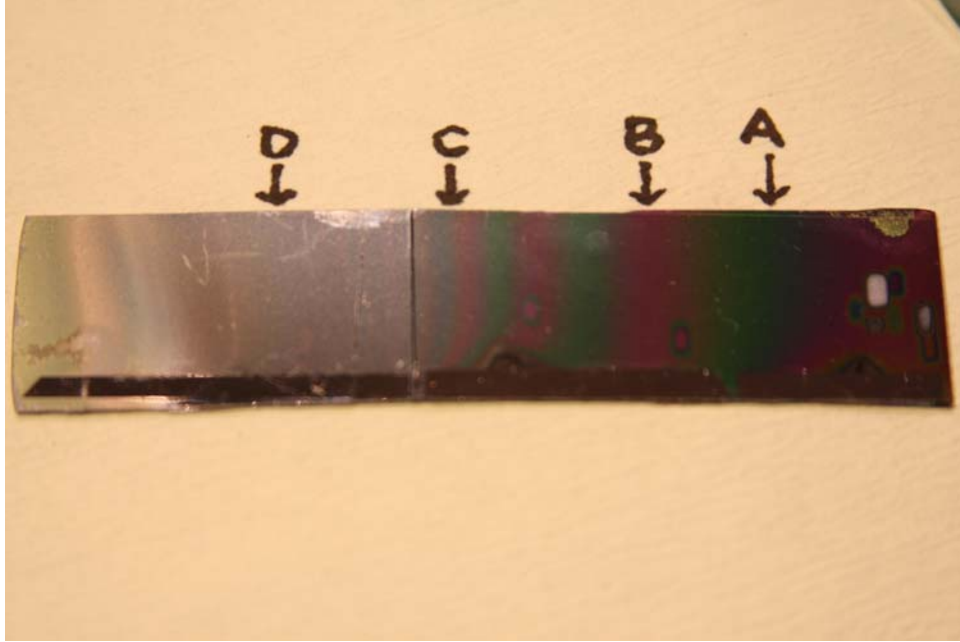

Figure 6.21: *A picture of Er-doped a-C:D with an increasing film thickness and Er concentration from right to left.*

Table 6.3: *Summary of atomic concentration results of Er-doped a-C:D sample.*

Spot	A	B	C	D
Distance away from Er reservoir (cm)	16	15	13	11
Er concentration at ~200 nm below surface (at.%)	0.47	0.75	1.39	2.29
O concentration at ~200 nm below surface (at.%)	5.11	8.16	11.19	13.87
Film thickness (μm)	0.45	0.58	0.86	2.0

Same approach used in the analysis of E7 was applied to the Er-doped a-C:D film to find out the minimum doping requirement to reveal Er luminescence in the sample. It happened to be 0.47 at.% (M_D) at spot A. Any spot on the film whose Er concentration is above 0.47 is able to exhibit room temperature Er luminescence. In contrast with M_H in case of Er doped a-C:H, M_D is ~ 4.4 times smaller. By deuterating Er-doped a-C:H, the efficiency of Er luminescence was surprisingly improved. The reason behind this has been discussed in section 6.5. However, the C-H bonds

originated from metal-organic ligands could still quench the Er emission, since they are very close to the Er^{3+} ion, provided that the metal-ligands bond did not break during the deposition.

As shown in Fig. 6.22, a broad and clear Er PL centered at 1545 nm is observed. As expected, the growth rate and the intensity of the Er luminescence increase with the Er concentration. This result implies that the high-solubility can be achieved without further quenching the Er emission due to Er cluster formation [25]. The surface quality at the spots (A, B and C) appears to be very good seem by naked eyes as seen in Fig. 21.

The bandgap of the Er-doped a-C:D film with a 1.5 at.% Er concentration was determined to be 2.65 eV as seen in Fig. 6.23. It appears to be higher than that of Er-doped a-C:H. This can be explain by the fact that deuterium can remove sates out the mid-gap and probably these states are less in deuterated carbon than in hydrogenated carbon [63]. Mathis et al. found that Tauc's gap for deuterated carbon is 20% higher than the hydrogenated carbon one for the same deposition parameters, while the density remained constant; incorporation of deuterium in carbon increases the Tauc energy.

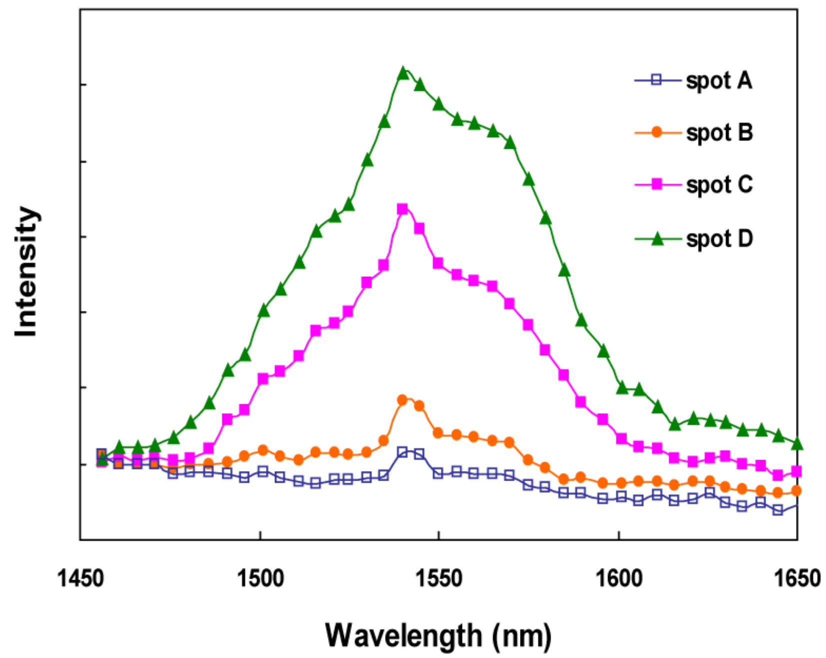

Figure 6.22: *PL spectra of four spots with different Er concentrations on Er-doped a-C:D film.*

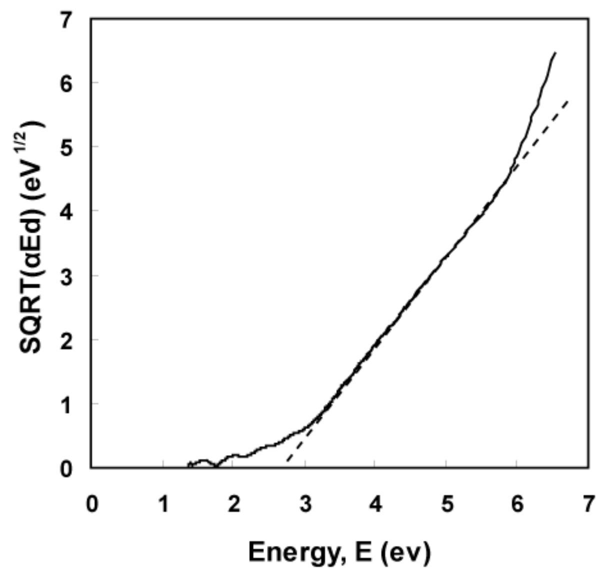

Figure 6.23: *Tauc plot of the Er-doped a-C:D film determines the optical bandgap.*

General conclusion and summary

Light emission from rare earth-doped matrices has been widely studied because of possible applications in optoelectronics. Of particular interest is erbium which in its Er3+ state emits at a wavelength near 1.54 μm that is close to the minimum absorption of optical fibers. Hydrogenated amorphous carbon (a-C:H) which has been explored much in this field, appears to be a great host candidate due to its flexibility in opto-electronic properties. However, common problems with Er-doped matrices are the low solubility of the Er^{3+} ion alone with the possibility of cluster formation and the low absorption cross-section of the Er^{3+} ion. These problems can be avoided by using Er-contained metal-organic complex. In this thesis, Er-doped a-C:H was fabricated by utilizing our unique DC saddle-field glow discharge deposition system. The deposition system was slightly modified to accommodate the needs for metal-organic doping method. By this method, the homogeneous doping distribution and the solubility of the Er^{3+} were achieved.

Frist, a suitable deposition conditions, used to prepare a high optical bandgap diamond-like carbon with good surface quality, have been established as listed in Table 4.1.

The suitability of two Er contained metal-organic complex, ($Er(acac)_3$ and $Er(TMHD)_3$), as an Er doing source were investigated. It turns out $Er(TMHD)_3$ is a better choice. The controlled sublimation of $Er(TMHD)_3$ occurred when heated above 125 ˚C during the deposition, while the sublimation of $Er(acac)_3$ only happened for

the most part in the first 10 minutes and 20% of amount loaded was evaporated, due to its poor thermal stability and unsaturated coordination of the Er^{3+} ion.

The SIMS results revealed the contaminations (Cr, K, Na and Ca) at the film-substrate interface caused by the Ar discharge pre-cleaning before the deposition. This was solved by installing a shutter assembly in between the substrate holder and discharge region.

$Er(TMHD)_3$ in diluted in KBr pellets exhibit strong broad-band Er emission centered at 1545 nm and its intensity increases with the Er concentration. This result has proven that this metal-organic material can potentially be used as a light-emitting site embedded in a solid matrix in light-generation applications.

Er-doped a-C:H films were prepared with different Er concentrations and XPS and SIMS analysis were carried out to determine chemical element concentrations as well as depth profiles. The Er distribution was homogeneous through film thickness confirming that the sublimed Er source system was delivering a constant flux of Er to the chamber during the growth period. The growth rate increase rapidly as the evaporator temperature raised above 145 ˚C; the metal-organic ligands dominated in the film growth as the corresponding Er concentration increased above 1.5 atom%. The thermal annealing did not improve the Er emission, in fact, it increases the background intensity which is attributed to the emission form the host material.

In spite of fact that high Er solubility can be achieved, the minimum value of the Er concentration required to reveal a detectable Er emission was as high as 2.04 at.%

for the films deposition with the gas mixture of methane and Er(TMHD)$_3$. The luminescence quenching effect was mainly due to the energy transfer between the excited Er^{3+} atom and the high frequency C-H and O-H oscillators. The comparison between the PL spectra of Er(TMHD)$_3$ dissolved in methanol and deuterated methanol suggests the deuteration of a-C:H, which eliminate the non-radiative quenching via vibrational excitation, could be a solution to reveal Er luminescence in a amorphous carbon film.

By substituting H with D, we have successfully show the Er luminescence in the deuterated amorphous carbon with the lowest Er concentration of 0.47 at.%, which is 4.4 times smaller than that in the case of the hydrogenated amorphous carbon. The film quality and the bandgap of the Er-doped a-C:D film appears to be sufficiently good. However, the deuteration is a lengthy process and still non-economical.

Future Work

In future work, the uniformity of the film can be improved by upgrading the delivering component of the evaporator. A shower head or gas ring should be added and connected to the outlet of the evaporator. The entire delivering component has to be heated to few tens of degree higher than the evaporator temperature to ensure a constant flux of sublimated metal-organic, at the same time no addition contamination sputtered from the heating element would be introduced into the discharge region.

There are two possible solutions to further enhance the Er luminescence. First, other exciting sources can be used to investigate efficiency of the indirect excitation

mechanism through transferring energy from metal-organic to Er^{3+} that is discussed in section 3.3. Secondly, the metal-organic complex can also be deuterated to further reduce the quenching mechanism induced by C-H and O-H vibrational excitation.

It would be very interesting to investigate the transport properties of a-C:H films. Conductivity in a-C:H can be achieved by doing with P or B. With this kind of film it would be possible to create a heterojunction which depends on the doping of a-C:H to demonstrate Er electroluminescence (EL).

Finally a further investigation about the influence of $Er(TMHD)_3$ doing on conductivity and bandgap of a-C:H films is also interesting because this directly affects the performance of the Er-related EL.

Reference

[1] Krishnamoorthy, Ashok V., Preceedings of SPIE – The International Society for Optical Engineering, V 6032, p. 603201 (2006).

[2] H. Ennen, J. Schneider, G. Pomrenke, and A. Axmann, Appl. Phys. Lett. **43**, 943 (1983).

[3] L. Tsybeskov, S. P. Duttagupta, K. D. Hirschman, P. M. Fauchet K. L. Moore and D. G. Hall Appl. Phys. Lett. **70**, 14 (1997).

[4] L. T. Canham, Appl. Phys. Lett. **57**, 1046 (1990)

[5] R. W. Collins, P. M. Fauchet, I. Shimizu, J. C. Vial, T. Shimada, and A. P. Alivisatos, Mater. Res. Soc. Symp. Proc. 452, (1996).

[6] J. C. Vial and J. Derrien, Porous Si Science and Technology (Springer, Berlin, 1995).

[7] Y. Kanemitsu, Phys. Rep. 263, 1 (1995).

[8] P.G. Kik and A. Polman, in "Towards the First Silicon Laser", L. Pavesi et al. (eds.), Kluwer Academic (2003), 383-400.

[9] F. Iacona et al., Appl. Phys. Lett., vol. 81, 3242-4, 2002.

[10] J. Lee, Jung H. Shin, and Namkyoo Park, Journal of Lightwave Tech., Vol. 23, NO. 1, 2005.

[11] R.A. Babunts, V.A. Vetrov, I.V. Ilin, E.N. Mokhov, N.G. Romanov, V.A. Khramtsov, and P.G. Baranov, Phys. Solid State **42**, 829 (2000).

[12] M. Markmann, E. Neufeld, A. Sticht, K. Brunner, and G. Abstreiter, Appl. Phys. Lett. **78**, 210 (2001).

[13] G. Speranza, L. Calliari, M. Ferrari, A. Chiasera, K. Tran Ngoc, A.M. Baranov, V.V. Sleptsov, A.A. Nefedov, A.E. Varfolomeev, S.S. Fanchenko, Appl. Surf. Science 238 (2004).

[14] S. Hufner, Optical spectra of transparent rare earth compounds (Academic, New York, 1978).

[15] R. S. Quimby, W. J. Miniscalco, B. Thompson, J. Appl. Phys. **76**, 4472 (1994).

[16] J. Robertson, Surf. Coat. Tech. 50, 185 (1992).

[17] H.O. Pierson, "Handbook of carbon, graphite, diamond and fullerenes", Noyes Publications (1993).

[18] A.H. Lettington, E-MRS "Amorphous hydrogenated carbon films", VolXVII, p.359-369, Les editions de physique (1987).

[19] M. Flynn, O.H.Y. Zalloum, J. Wojcik, I. Calder, S. Gujrathi, Steven Hill and P. Mascher, 3rd IEEE International Conference on Group IV Photonics, 2006, p 3 pp.
[20] N A Feoktistov, V G Golubev, A V Medvedev and A B Pevtsov, Semicond. Sci. Technol. **16** (2001) 54–57.
[21] W. Q. Zhao, P. F. Wang, at el., J. Phys. D: Appl. Phys. **39** (2006) 2711-2714.
[22] A. J. Kenyon, Semicond. Sci. Technol. **20** (2005) R65-R84.
[23] F. Priolo, S. coffa, g. Franzo, C. Spinella, A. Carnera, and V. Vallani, J., Appl. Phys. **74**, 4936 (1993).
[24] D. B. Beach, R. T. Collions, F. K. Legoues, and J. O. Chu, Mater. Res. Soc. Symp. Proc. **282**, 897 (1992).
[25] Francesco Priolo, Giorgia Franzò, Domenico Pacifici, and Vincenzo Vinciguerra, J. Appl. Phys., Vol. 89, No. 1, 1 January 2001
[26] Seunghoon Lee, Ung Kim, Juntae Kim and Sang Man Koo, Mat. Res. Soc. Symp. Proc. Vol. 817 (2004).
[27] Weissman S.I., J. Chem. Phys. 1942, **10**, 214.
[28] Forsberg J.H., in Gmelin Handbook of Inorganic Chemistry, Sc, Y, La-Lu Rare Earth Elements, System Nr. 39, Vol. D3, Springer-Verlag, Berlin 1981, 65-251 and references therein.
[29] Drake S.R., Lyons N.J., Otway D.J., Slawin A.M.Z., Willimans D.J., J. Chem. Soc., Dalton Trans. 1993, **15**, 2379.
[30] G.A. Crosby and M. Kasha, Spectrochim. Acta, **10** (1958) 377.
[31] R.E. Whan and G.A. Crosby, J. Mol. Spectrosc., **8** (1962) 315.
[32] M. Kleinerman, Bull. Am. Phys. Sot., 9 (1964) 265 J. Chem. Phys., **51** (1969) 2370.
[33] N.I. Giricheva, N.V. Belova, S.A. Shlykov, G.V. Girichev, N. Vogt, N.V. Tverdova, J. Vogt, Journal of Molecular Structure **605** (2002) 171-176
[34] R. F. Bunshah, Handbook of Deposition Technologies for Films and Coatings (Noyes Publications, Park Bridge, 1993).
[35] A. M. Howatson, An Introduction to Gas Discharges (Pergamon Press, Oxford, 1976).
[36] Y. R. Raizer, Gas Discharge Physics (Springer-Verlag, Berlin, 1991).
[37] D. L. Smith, Thin Film Deposition (McGraw-Hill, Inc, New York, 1994).
[38] R. V. Kruzelecky, S. Zukotynski, S, Mat Sci Forum. **140-142**, 89 (1993).
[39] A. M. Mcllraith, Nature **212**, 1422 (1966).
[40] R. V. Kruzelecky, S. Zukotynski, C. I. Ukah, F. Gaspari, and J. M. Perz, J. Vac. Sci. Tech. **A 7**, 2632 (1989).
[41] P. K. Lim, F. Gaspari, and S. Zukotynski, J. Appl. Phys. **78**, 5307 (1995).

[42] J. Franks, Vacuum **34**. 259 (1984).
[43] Sagnes, E., Ph.D. Thesis, Department of Electrical and Computer Engineering, University of Toronto (1998).
[44] Vaclav Prajzlera, Ivan Huttel, Pavla Nekvindova, Josef Schrfel, Anna Mackova, Jan Gurovic. Thin Solid Films. **433,** (2003) 363–366.
[45] K. Kuratani, M. Mizuhata, A. Kajinami, S. Deki, J. Alloys Compd. 408–412 (2006) 711.
[46] Hare Ram Aryal, Sudip Adhikari, Dilip Chandra Ghimire, Golap Kalita, Masayoshi Umeno, Diamond & Related Materials **17** (2008) 680–683
[47] Jun Xu, Tianfu Ma, Wei Li, Kunji chen, Jiafang Du, Xinfan Huang, Journal of Non-Crystalline Solids 266-269 (2000) 769-772.
[48] Pradhan D, Sharon M, Applied Surface Science, v 253, n 17, 30 June 2007, 7004-10.
[49] R. A. Street, *Hydrogenated amorphous Silicon* (Cambridge University Press, Cambridge, 1991).
[50] G. D. Cody, T. Tiedje, B. Abeles, b. Brooks, and Y. Glodstein, Phys, Rev. Lett. **47**, 1480 (1981).
[50] F. Demichelis, g. Kanidakis, A. Tagliaferro, and E. Tresso, Applied Optics, **26**, 1737 (1987).
[52] J. F. Moulder, W. F. Stickle, P. E. Sobol, and D. D. Bomben, *Handbook of X-ray Photoelectron Spectroscopy* (Perkin Elmer Corporation, 1992).
[53] Rana N. S. Sodhi, "Time-of-flight Secondary Ion Mass spectrometry (TOF-SIMS):- versatility in chemical and imaging surface analysis." Analyst vol. 129, (2004) p.483.
[54] Milton Ohring, Materials Science of Thin Films 2nd ed., Academic Press, New York, 2002.
[55] L.I. Martynenko, Visokochistye Veschestva, (1) (1987) 88.
[56] I.G. Zaitzeva et al., Journal of Allys and Compounds **225** (1995) 303-395
[57] Shuhan Lin and Bernard J. Feldman, Solid State Communications, Vol. 80, No. 6, pp. 371-372, 1991.
[58] Ichiro Watanabe et al., Jap. Journal of Appl. Phys. Vol. 21, No. 6, June, pp. 856-859, 1982.
[59] A. Foulani, J. Phys. D: Appl. Phys. **36** (2003) 394-398.
[60] N.M.J. Conway et al., Diamond and Related Material **9** (2000) 765-770.
[61] J. L Rogers, E. Adams, P. B. Klein et al., J. Appl. Phys. **78** (1995) 10.
[62] V. L. Ermolaev and E. B. Sveshnikova, Russ. Chem. Rev. **63**, 905 _1994.
[63] N. Mathis, C. Meunier, F. Munnik, S. Mikhailov, Thin Solid Films **516** (2008) 1508 – 1511.